Drug Design, Development and Therapy

Dovepress
Taylor & Francis Group

Open Access Full Text Article

ORIGINAL RESEARCH

Design, Synthesis and Anti-Inflammation Evaluation of *N*-Acyl Tryptophan Derivatives as Promising $P2Y_{14}R$ Antagonists Against Lipopolysaccharide-Induced Acute Lung Injury

Bingqian Han[1,2,*], Shiyu Ma[3,*], Wenjin Liu[2,*], Yuyang Wang[2,*], Mingzhu Wang[1], Yuanzhe Li[1], Chuanjun Song[3], Yongfang Yao[1–3], Moran Sun[2], Yongtao Duan[1]

[1]Henan Provincial Key Laboratory of Pediatric Hematology, Children's Hospital Affiliated to Zhengzhou University, Zhengzhou University, Zhengzhou, Henan, People's Republic of China; [2]School of Pharmaceutical Science, Zhengzhou University, Zhengzhou, Henan, People's Republic of China; [3]College of Chemistry, Pingyuan Laboratory, Zhengzhou University, Zhengzhou, Henan, People's Republic of China

*These authors contributed equally to this work

Correspondence: Yongtao Duan; Moran Sun, Henan Provincial Key Laboratory of Pediatric Hematology, Children's Hospital Affiliated to Zhengzhou University, Zhengzhou University, Zhengzhou, Henan, 450018, People's Republic of China, Email duanyongtao860409@163.com; sunmr@zzu.edu.cn

Purpose: The $P2Y_{14}$ receptor ($P2Y_{14}R$) is closely associated with several inflammatory diseases in humans. Although several $P2Y_{14}R$ antagonists have been reported to date, few have been successfully developed as therapeutic drugs, and none have entered clinical trials. We aimed to obtain $P2Y_{14}R$ antagonists with high antagonistic activity and druggability for further investigation into anti-inflammatory drugs.

Methods: Three series of novel $P2Y_{14}R$ antagonists were screened. The druggability of the most promising compounds was evaluated through assays for the inhibition of cytochrome P450 and hERG (human Ether-à-go-go-Related Gene) channels, as well as pharmacokinetic experiments. The in vivo efficacy of the lead compound was assessed in a Lipopolysaccharide (LPS)-induced acute lung injury (ALI) mouse model.

Results: We designed a series of *N*-acyl tryptophan derivatives as novel and potent $P2Y_{14}R$ antagonists based on the hit compound **7**. Among them, compound **II-3** with an IC_{50} value of 1.2 nM, was a better antagonist than **PPTN** with an IC_{50} value of 2.0 nM. Through structural modification, the zwitterionic character was eliminated, resulting in significantly improved solubility and oral bioavailability compared to PPTN. We have confirmed that $P2Y_{14}R$ is highly expressed in macrophages of ALI lung tissue. II-3, as a $P2Y_{14}R$ antagonist, can alleviate the pathological progression of ALI by inhibiting the activation of the NLRP3 inflammasome pathway and reducing the release of inflammatory factors, thus providing direct evidence for $P2Y_{14}R$ as a therapeutic target.

Conclusion: Compound **II-3** with potent $P2Y_{14}R$ antagonistic activity, may be a promising candidate for further investigation as an anti-inflammatory drug.

Keywords: $P2Y_{14}$ receptor, antagonist, G protein-coupled receptor, *N*-acyl tryptophan derivatives, anti-inflammatory activity

Introduction

When the body is under pressure or injured, specific tissues or organs can release various important intracellular molecules into the extracellular fluid.[1,2] These extracellular nucleotides can interact with at least 15 different cell surface receptors to regulate cellular signaling and physiological responses.[3] These receptors have been identified as purinergic receptors and are mainly divided into adenosine (P1) and nucleotide (P2) receptors.[4] The P2 family is further divided into two subfamilies: P2X and P2Y receptors.[5,6] As a subtype of P2Y receptors, the $P2Y_{14}$ receptor ($P2Y_{14}R$) is a G protein-coupled receptor (GPCR) that can be activated by extracellular UDPG, $P2Y_{14}R$ is expressed in a variety of tissues,

Received: 30 October 2024
Accepted: 9 August 2025
Published: 20 August 2025

particularly in epithelial and immune cells. Its activation is closely linked to intracellular signaling pathways and plays a significant role in modulating immune responses and inflammatory processes.[7–9] Mechanistically, $P2Y_{14}R$ activation triggers Gi-mediated inhibition of adenylate cyclase (AC), thereby suppressing intracellular cAMP production and modulating downstream signaling cascades.[10–12] This receptor demonstrates pathological significance across multiple inflammatory disorders: In acute gouty arthritis, it exacerbates disease progression by promoting NLRP3 inflammasome-dependent macrophage pyroptosis.[13,14] In ulcerative colitis, $P2Y_{14}R$ overexpression in intestinal epithelium drives disease severity through programmed necroptosis, with genetic ablation ameliorating colitis symptoms in preclinical models.[15] Moreover, $P2Y_{14}R$ exerts key regulatory functions in a variety of pathological processes, including diabetes,[16] cystic fibrosis,[17] and allergic diseases.[18] Recent studies have shown that the activation of $P2Y_{14}R$ by endogenous UDPG leads to neutrophil recruitment and increased inflammation, whereas $P2Y_{14}R$ antagonists reduce inflammation in renal intercalated cells.[19,20] In addition, $P2Y_{14}R$ exists in the central nervous system, inhibiting the release of matrix metalloproteinase-9 (MMP-9) and tumor necrosis factor (TNF) from astrocytes.[21] It's worth noting that $P2Y_{14}R$ antagonists significantly reduce lung inflammation and tissue damage in acute lung injury (ALI) by inhibiting the activation of NLRP3 inflammatory body signaling pathway and reducing the release of inflammatory factors and immune cell infiltration.[22] Therefore, $P2Y_{14}R$ is a potential target for the treatment of inflammation. The LPS-induced ALI model holds significant value in anti-inflammatory research, it simulates the acute inflammatory phase of ARDS related to sepsis or COVID-19, offering substantial translational medicine value. Therefore, the ALI model was selected in this study to verify the in vivo efficacy of $P2Y_{14}R$ antagonists.[22] To date, only a few $P2Y_{14}R$ antagonists with different skeletal structures have been reported. Initially, the Black group reported a series of weak $P2Y_{14}R$ antagonists containing dihydropyridopyrimidine structures, and compound **1** showed the best antagonistic activity among them.[23] However, further research has not been conducted on dihydropyridopyrimidine derivatives because they have serious side effects in the human body. Subsequently, the Black group reported 7-phenyl-2-naphthoic acid derivative **2**, which is an effective, high-affinity, competitive, and highly selective $P2Y_{14}R$ antagonist, well-known as **PPTN**.[24,25] Jacobson and Hu further proposed bioisosteric alternatives to hydrophobic and rigid naphthalene rings, namely, compounds **3, 4**, and.[26,27] However, these compounds have poor solubility and low oral bioavailability because of their high lipophilicity and zwitterionic properties (Please refer to Table 1 for the explanation of professional vocabulary), which make their application in medicine difficult. In recent years, Jacobson group has focused on modifying the piperidine ring with zwitterionic characteristics on the basis of **PPTN**, that is, enhancing the spatial constraints on the piperidine ring and bridging the piperidine ring, compound **6** is one example as shown in Figure 1.[28] In 2020, Hu et al reported a series of hit compounds of $P2Y_{14}R$ with novel scaffolds using a Glide-docking-based virtual screening (VS) strategy. Compound **7** eliminated the zwitterionic characteristics and had considerable antagonistic activity compared to other hit compounds.[29] Hu et al further modified compound **5** to obtain compound **8**, which eliminated the zwitterionic characteristics and

Table 1 Glossary

Term	Definition
Zwitterionic Characteristics	Molecules that have both positive and negative charges simultaneously, making them neutral overall, highly water-soluble.
Bioisosteric Alternatives	Compounds or functional groups that have similar physical or chemical properties and can replace each other in a molecule without significantly altering its biological activity.
Solubility Enhancement	Making a substance more soluble in a particular liquid.
Spatial Constraints	Physical limitations or restrictions imposed by the three-dimensional arrangement of atoms, molecules, or structures, which influence their interactions, reactivity, or functionality.
Bioavailability	The proportion of a drug or substance that enters circulation and becomes available at the target site to exert its biological effect after administration.

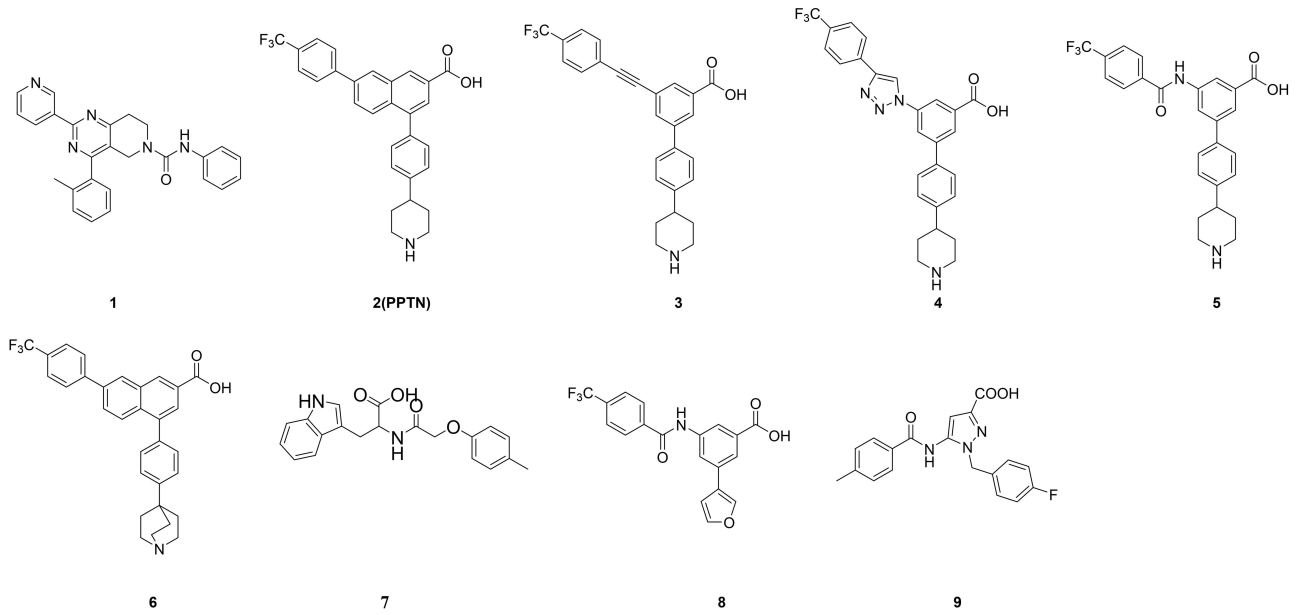

Figure 1 Representative chemical structures of reported $P2Y_{14}R$ antagonists.

significantly improved the solubility and bioavailability of $P2Y_{14}R$ antagonists.[14] Afterwards, Jiang et al designed and synthesized a series of 5-amide-1*H*-pyrazole-3-carboxyl derivatives and obtained the novel, easily synthesized, and potent $P2Y_{14}R$ antagonist compound **9**.[30] Recently, different studies employed computational methods to investigate novel skeleton compounds and molecular interactions. Common methods include docking, MD, and MM-PBSA, while enhanced sampling (umbrella/steered MD) addresses specific binding/unbinding dynamics. GROMACS and MM-PBSA are central across studies, with tailored approaches (HADDOCK, DFT optimization) for system-specific challenges. These workflows highlight integrative computational strategies for drug design and biophysical analysis.[31–33]

Although many new $P2Y_{14}R$ antagonists have been reported in recent years, there have been no reports of $P2Y_{14}R$ antagonists entering clinical trial. Compound **7** exhibited significant antagonistic activity, but its poor bioavailability (F = 6%) limited its clinical application. Therefore, Based on molecular docking insights, we hypothesized that modifying the carboxylic acid moiety and introducing ester prodrugs could eliminate zwitterionic interactions and enhance solubility. This rationale guided the design of three series of N-acyl tryptophan derivatives, aiming to balance antagonistic potency with druggability. We aimed to obtain $P2Y_{14}R$ antagonists with high antagonistic activity and druggability for further investigation into anti-inflammatory drugs.[29] This not only continues the previous achievements of Jacobson, Hu and other teams, but also provides compelling evidence for the critical pro-inflammatory role of $P2Y_{14}R$ in ALI. This study is the first to combine single-cell profiling to analyze the spatial distribution and function of $P2Y_{14}R$ in ALI, revealing that II-3, as a $P2Y_{14}R$ antagonist, alleviates the therapeutic effect of ALI through dual mechanisms (inhibition of immune cell infiltration and the NLRP3 pathway).

Materials and Methods

Chemical Synthesis

All chemical reagents and solvents were commercially available and used without further purification. All reactions were monitored by thin-layer chromatography (TLC) using 254 nm fluorescent indicators. The silica gel used for column chromatography (CC) was 200–300 mesh, produced by Shandong Xinnuo New Material Technology Co., Ltd. Bruker 400 MHz or 600 MHz NMR instruments (^1H = 400 MHz and 600 MHz, ^{13}C = 101MHz) were used to determine the hydrogen and carbon spectra of, using $CDCl_3$-*d* or DMSO-d_6 as solvents (TMS was the internal standard at 25 °C). High-resolution mass spectroscopy (HRMS) data were recorded on an Orbitrap Exploris 120 mass spectrometer. Melting

 https://doi.org/10.2147/DDDT.S497291

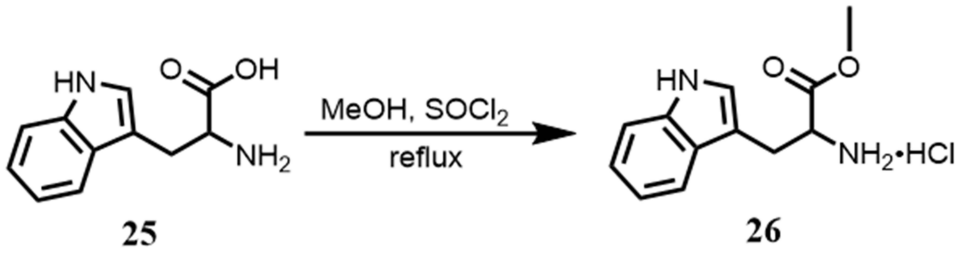

Figure 2 General procedure for the synthesis of **26** (Method A).

points were detected using an XT4A micro-melting point apparatus (Beijing Scientific Instruments Electrooptic Instrument Factory).

General Procedure for the Synthesis of 26 (Method A)

Compound **25** (200 mg, 0.9792 mmol, 1.0 equiv) was dissolved in 15mL methanol. After the addition of $SOCl_2$ (278 μL, 3.9168 mmol, 4.0 eq), the ice bath was removed and the reaction was stirred at high temperature under reflux conditions. When the reaction was complete, the solvent and remaining $SOCl_2$ were dried under reduced pressure to obtain intermediate **26**. The product was directly added to the subsequent reaction step. **27** and **28** were synthesized using the same procedure (Figure 2).

Procedure for the Synthesis of II-1 (Method B)

2-(*p*-Tolyloxy)acetic acid (100 mg, 0.5993 mmol, 1.0 equiv) was dissolved in CH_2Cl_2 (10 mL). EDCI (144 mg, 0.7192 mmol, 1.2 equiv) and HOBt (91 mg, 0.7192 mmol, 1.2 equiv) were added. The mixture was then stirred at ambient temperature for 20 min. Et_3N (166 μL, 1.1986 mmol, 2.0 equiv) and **26** (170 mg, 0.5993 mmol, 1.0 equiv) were added. The reaction was monitored using thin-layer chromatography (TLC). After the completion of the reaction was complete, 5 mL CH_2Cl_2 was added. The mixture was then washed with 20 mL of distilled water. The separated aqueous phase was extracted with CH_2Cl_2 (2×25 mL). The combined organic phases were washed with brine (3×10 mL), dried over anhydrous magnesium sulfate, filtered, and concentrated under reduced pressure. The residue was purified using silica gel column chromatography (petroleum ether/ethyl acetate = 3:1) to yield **II-1. II-2~II-3, III-1~III-22 and 10~24** were synthesized using the same procedure (Figure 3).

Procedure for the Synthesis of the Hit Compound 7 (Method C)

Compound **II-1** (100 mg, 0.2760 mmol, 1.0 equiv) was dissolved in methanol, and 2M NaOH solution (567μL, 1.1040 mmol, 4.0 eq) was added to the reaction system. The mixture was heated to 65 °C. After the reaction was complete, 1 M HCl was added until a pH of 2–3 was the precipitated precipitate was filtered. The filter cake was washed successively with water (5 mL) and CH_2Cl_2 (2 mL), and then dried to obtain compound **7. I-1~I-15** were synthesized using the same procedure (Figure 4).

Procedure for the Synthesis of II-4 (Method D)

Compound **7** (100 mg, 0.2838 mmol, 1.0 equiv) was dissolved in CH_2Cl_2 (5 mL). DCC (72 mg, 0.3406 mmol, 1.2 equiv), DMAP (46 mg, 0.3406 mmol, 1.2 equiv) and benzyl alcohol (30 μL, 0.2838 mmol, 1.0 equiv) were added. The reaction

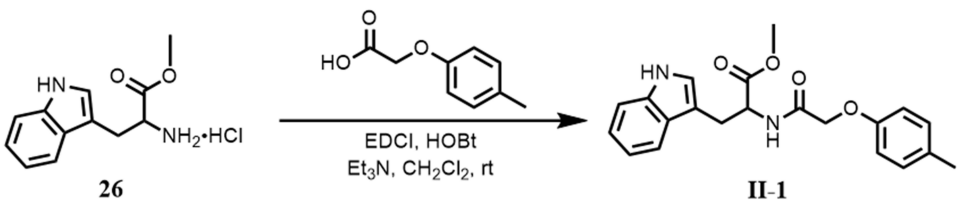

Figure 3 Procedure for the synthesis of **II-1** (Method B).

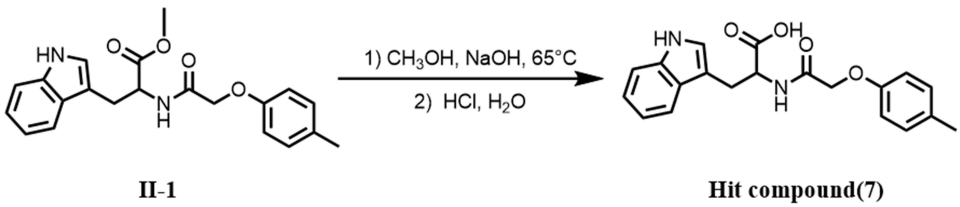

Figure 4 Procedure for the synthesis of the hit compound **7** (Method C).

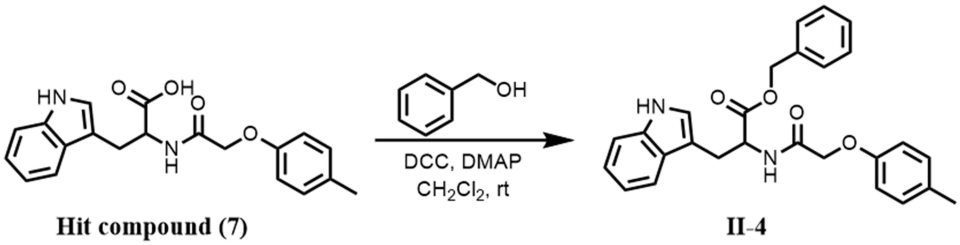

Figure 5 Procedure for the synthesis of **II-4** (Method D).

mixture was stirred at ambient temperature until completion as monitored by TLC. 25 mL CH_2Cl_2 was added to dilute the solution. The system was then washed once with 20 mL of distilled water, and the aqueous phase was extracted twice with 25 mL of CH_2Cl_2. The organic phases were collected and washed three times with 10 mL of saturated salt water, dried with anhydrous magnesium sulfate, concentrated under reduced pressure, and subjected to silica gel column chromatography (petroleum ether/ethyl acetate = 2:1) to obtain **II-4**. Compound **II-5** was synthesized using the same procedure (Figure 5).

(2-Phenoxyacetyl)tryptophan (I-1)

Method C: White solid; yield: 85.3%. HPLC purity: 100%. m.p. 154.3–155.7 °C. ^{1}H NMR (400 MHz, DMSO-d_6) δ 12.82 (s, 1H), 10.89 (s, 1H), 8.21–8.06 (m, 1H), 7.61–7.51 (m, 1H), 7.40–7.33 (m, 1H), 7.32–7.21 (m, 2H), 7.17–7.11 (m, 1H), 7.11–7.03 (m, 1H), 7.03–6.92 (m, 2H), 6.90–6.79 (m, 2H), 4.63–4.52 (m, 1H), 4.47 (s, 2H), 3.29–3.11 (m, 2H). ^{13}C NMR (101 MHz, DMSO-d_6) δ 172.99, 167.53, 157.52, 136.05, 129.40, 127.16, 123.67, 121.10, 120.91, 118.39, 118.12, 114.58, 111.38, 109.52, 66.47, 52.55, 26.74. HRMS (ESI$^+$) m/z calculated for $C_{19}H_{18}N_2O_4$ $[M + H]^+$ 339.1339, found 339.1339.

(2-(4-Methoxyphenoxy)acetyl)tryptophan (I-2)

Method C: White solid; yield: 84.9%. HPLC purity: 100%. m.p. 160.1–161.5 °C. ^{1}H NMR (400 MHz, DMSO-d_6) δ 12.84 (s, 1H), 10.92 (s, 1H), 8.17–8.00 (m, 1H), 7.63–7.48 (m, 1H), 7.42–7.29 (m, 1H), 7.15 (s, 1H), 7.13–7.05 (m, 1H), 7.05–6.93 (m, 1H), 6.89–6.71 (m, 4H), 4.67–4.50 (m, 1H), 4.50–4.28 (m, 2H), 3.70 (s, 3H), 3.30–3.07 (m, 2H). ^{13}C NMR (101 MHz, DMSO-d_6) δ 172.94, 167.72, 153.75, 151.60, 136.08, 127.20, 123.72, 120.91, 118.40, 118.15, 115.64, 114.47, 111.35, 109.52, 67.44, 55.37, 52.51, 26.75. HRMS (ESI$^+$) m/z calculated for $C_{20}H_{20}N_2O_5$ $[M + H]^+$ was 369.1445 and 369.1446.

(2-(4-Fluorophenoxy)acetyl)tryptophan (I-3)

Method C: White solid, 80.5% yield. HPLC purity: 100%. m.p. 159.1–160.7 °C. ^{1}H NMR (400 MHz, DMSO-d_6) δ 12.83 (s, 1H), 10.91 (s, 1H), 8.17 (d, J = 8.0 Hz, 1H), 7.56 (d, J = 7.9 Hz, 1H), 7.39–7.30 (m, 1H), 7.19–7.12 (m, 1H), 7.12–7.04 (m, 3H), 7.03–6.93 (m, 1H), 6.90–6.80 (m, 2H), 4.62–4.52 (m, 1H), 4.45 (s, 2H), 3.30–3.07 (m, 2H). ^{13}C NMR (101 MHz, DMSO-d_6) δ 172.93, 167.41, 156.75 (d, $J_{F\text{-}C}$ = 237.2 Hz), 153.93, 136.07, 127.18, 123.71, 120.91, 118.39, 118.10, 115.99 (d, $J_{F\text{-}C}$ = 8.1 Hz), 115.7 (d, $J_{F\text{-}C}$ = 22.2 Hz), 111.34, 109.56, 67.18, 52.60, 26.76. HRMS (ESI$^+$) m/z values calculated for $C_{19}H_{17}FN_2O_4$ $[M + H]^+$ 357.1245, 357.1247.

https://doi.org/10.2147/DDDT.S497291

(2-(4-Chlorophenoxy)acetyl)tryptophan (I-4)

Method C: White solid; yield: 84.6%. HPLC purity: 100%. m.p. 138.7–139.6 °C. ^{1}H NMR (400 MHz, DMSO-d_6) δ 12.83 (s, 1H), 10.89 (s, 1H), 8.20 (d, J = 8.0 Hz, 1H), 7.56 (d, J = 7.9 Hz, 1H), 7.39–7.33 (m, 1H), 7.33–7.23 (m, 2H), 7.19–7.13 (m, 1H), 7.12–7.03 (m, 1H), 7.02–6.93 (m, 1H), 6.90–6.80 (m, 2H), 4.64–4.53 (m, 1H), 4.48 (s, 2H), 3.29–3.05 (m, 2H). ^{13}C NMR (101 MHz, DMSO-d_6) δ 172.98, 167.23, 156.44, 136.05, 129.10, 127.15, 124.76, 123.67, 120.91, 118.40, 118.13, 116.35, 111.37, 109.59, 66.71, 52.62, 26.76. HRMS (ESI$^+$) m/z calculated for $C_{19}H_{17}ClN_2O_4$ [M + H] $^+$ 373.0950, 373.0948.

(2-(4-Bromophenoxy)acetyl)tryptophan (I-5)

Method C: White solid; yield: 83.9%. HPLC purity: 96.40%. m.p. 165.7–166.9 °C. ^{1}H NMR (400 MHz, DMSO-d_6) δ 12.96 (s, 1H), 10.89 (s, 1H), 8.19 (d, J = 7.7 Hz, 1H), 7.56 (d, J = 7.7 Hz, 1H), 7.45–7.30 (m, 3H), 7.15 (s, 1H), 7.12–7.03 (m, 1H), 7.03–6.90 (m, 1H), 6.86–6.74 (m, 2H), 4.65–4.50 (m, 1H), 4.48 (s, 2H), 3.31–3.07 (m, 2H). ^{13}C NMR (101 MHz, DMSO-d_6) δ 172.98, 167.12, 156.92, 136.06, 132.01, 127.23, 123.69, 120.89, 118.37, 118.12, 116.90, 112.53, 111.35, 109.66, 66.75, 52.75, 26.82. The HRMS (ESI$^+$) m/z calculated for $C_{19}H_{17}BrN_2O_4$ [M + H] $^+$ 417.0444 was found to be 417.0447.

(2-(4-Formylphenoxy)acetyl)tryptophan (I-6)

Method C: White solid; yield: 73.4%. HPLC purity: 100%. m.p. 160.4–161.9 °C. ^{1}H NMR (400 MHz, DMSO-d_6) δ 12.86 (s, 1H), 10.89 (s, 1H), 9.87 (s, 1H), 8.32 (d, J = 8.0 Hz, 1H), 7.86–7.76 (m, 2H), 7.57 (d, J = 7.9 Hz, 1H), 7.39–7.33 (m, 1H), 7.16 (s, 1H), 7.12–7.04 (m, 1H), 7.05–6.94 (m, 3H), 4.63 (s, 2H), 4.61–4.54 (m, 1H), 3.32–3.08 (m, 2H). ^{13}C NMR (101 MHz, DMSO-d_6) δ 191.24, 172.93, 166.87, 162.48, 136.08, 131.59, 130.01, 127.18, 123.70, 120.91, 118.40, 118.10, 115.04, 111.38, 109.59, 66.59, 52.71, 26.83. HRMS (ESI$^+$) m/z calculated for $C_{20}H_{18}N_2O_5$ [M + H] $^+$ 367.1288, 367.1289.

(2-(4-(Trifluoromethyl)phenoxy)acetyl)tryptophan (I-7)

Method C: White solid; yield: 70.6%. HPLC purity: 100%. m.p. 175.4–176.3 °C. ^{1}H NMR (400 MHz, DMSO-d_6) δ 12.86 (s, 1H), 10.89 (s, 1H), 8.30 (d, J = 8.0 Hz, 1H), 7.62–7.52 (m, 3H), 7.35 (d, J = 8.1 Hz, 1H), 7.19–7.13 (m, 1H), 7.11–7.03 (m, 1H), 7.02–6.93 (m, 3H), 4.58 (s, 2H), 4.57–4.52 (m, 1H), 3.28–3.08 (m, 2H). ^{13}C NMR (101 MHz, DMSO-d_6) δ 172.99, 166.92, 160.44, 136.08, 127.21, 126.77, 124.44 (q, $J_{F\text{-}C}$ = 272.1 Hz), 123.72, 121.58 (q, $J_{F\text{-}C}$ = 32.2 Hz), 120.88, 118.38, 118.12, 115.09, 111.34, 109.67, 66.55, 52.74, 26.86. HRMS (ESI$^+$) m/z values calculated for $C_{20}H_{17}F_3N_2O_4$ [M + H] $^+$ 407.1213, 407.1215.

(Furan-2-Carbonyl)tryptophan (I-8)

Method C: white solid; yield: 78.0%. HPLC purity: 98.66%. m.p. 169.9–171.2 °C. ^{1}H NMR (400 MHz, DMSO-d_6) δ 12.73 (s, 1H), 10.81 (s, 1H), 8.37 (d, J = 8.1 Hz, 1H), 7.81 (s, 1H), 7.56 (d, J = 7.9 Hz, 1H), 7.35–7.29 (m, 1H), 7.18–7.14 (m, 1H), 7.14–7.10 (m, 1H), 7.09–7.01 (m, 1H), 6.70–6.92 (m, 1H), 6.63–6.57 (m, 1H), 4.68–4.59 (m, 1H), 3.29–3.16 (m, 2H). ^{13}C NMR (101 MHz, DMSO-d_6) δ 173.27, 157.63, 147.35, 145.13, 136.03, 127.06, 123.53, 120.91, 118.34, 118.10, 113.79, 111.82, 111.39, 110.12, 52.76, 26.53. HRMS (ESI$^+$) m/z calculated for $C_{16}H_{14}N_2O_4$ [M + H] $^+$ 299.1026, 299.1028.

(Thiophene-2-Carbonyl)tryptophan (I-9)

Method C: White solid; yield: 75.9%. HPLC purity: 98.56%. m.p. 168.1–169.4 °C. ^{1}H NMR (400 MHz, DMSO-d_6) δ 12.71 (s, 1H), 10.80 (s, 1H), 8.67 (d, J = 8.1 Hz, 1H), 7.85–7.80 (m, 1H), 7.77–7.71 (m, 1H), 7.59 (d, J = 7.8 Hz, 1H), 7.35–7.29 (m, 1H), 7.20–7.16 (m, 1H), 7.16–7.11 (m, 1H), 7.09–7.02 (m, 1H), 7.01–6.94 (m, 1H), 4.70–4.55 (m, 1H), 3.29–3.11 (m, 2H). ^{13}C NMR (101 MHz, DMSO-d_6) δ 173.40, 161.14, 139.39, 136.06, 130.96, 128.52, 127.86, 127.09, 123.54, 120.94, 118.39, 118.12, 111.41, 110.30, 53.53, 26.72. HRMS (ESI$^+$) m/z calculated for $C_{16}H_{14}N_2O_3S$ [M + H] $^+$ 315.0798; observed: 315.0800.

4.1.10. *(thiazole-4-carbonyl)tryptophan* ***(I-10)***. Method C: White solid; yield: 81.5%. HPLC purity: 97.76%. m.p. 169.2–170.3 °C. ^{1}H NMR (400 MHz, DMSO-d_6) δ 12.91 (s, 1H), 10.85 (s, 1H), 9.14 (s, 1H), 8.38–8.29 (m, 1H), 8.22 (d, J = 8.0 Hz, 1H), 7.52 (d, J = 7.9 Hz, 1H), 7.36–8.28 (m, 1H), 7.19–7.10 (m, 1H), 7.09–7.01 (m, 1H), 6.98–6.89 (m, 1H),

4.81–4.66 (m, 1H), 3.31 (s, 2H). ^{13}C NMR (101 MHz, DMSO-d_6) δ 172.94, 160.07, 155.03, 150.14, 136.07, 127.23, 124.47, 123.57, 120.94, 118.35, 111.36, 109.52, 52.67, 26.73. HRMS (ESI$^+$) m/z calculated for $C_{15}H_{13}N_3O_3S$ [M + H] $^+$ 316.0750 found that 316.0752.

(Benzo[B]thiophene-2-Carbonyl)tryptophan (I-11)

Method C: White solid; yield: 76.4%. HPLC purity: 98.93%. m.p. 148.1–149.3 °C. ^{1}H NMR (400 MHz, DMSO-d_6) δ 12.74 (s, 1H), 10.81 (s, 1H), 8.97 (d, J = 8.0 Hz, 1H), 8.18 (s, 1H), 8.03–7.98 (m, 1H), 7.97–7.91 (m, 1H), 7.61 (d, J = 7.8 Hz, 1H), 7.50–7.39 (m, 2H), 7.35–7.28 (m, 1H), 7.24–7.18 (m, 1H), 7.09–7.02 (m, 1H), 7.02–6.95 (m, 1H), 4.71–4.59 (m, 1H), 3.38–3.15 (m, 2H). ^{13}C NMR (101 MHz, DMSO-d_6) δ 173.30, 161.52, 140.17, 139.38, 139.06, 136.04, 127.03, 126.24, 125.20, 124.90, 123.57, 122.77, 120.92, 118.08, 111.40, 118.37, 110.21, 53.75, 26.66. HRMS (ESI$^+$) m/z calculated for $C_{20}H_{16}N_2O_3S$ [M + H] $^+$ 365.0954, 365.0957.

(Benzo[D][1,3]dioxole-5-Carbonyl)tryptophan (I-12)

Method C: White solid; yield: 77.0%. HPLC purity: 100%. m.p. 146.1–147.5 °C. ^{1}H NMR (400 MHz, DMSO-d_6) δ 12.63 (s, 1H), 10.80 (s, 1H), 8.46 (d, *J* = 7.8 Hz, 1H), 7.58 (d, *J* = 7.8 Hz, 1H), 7.42 (dd, *J* = 8.2, 1.5 Hz, 1H), 7.36 (d, *J* = 1.4 Hz, 1H), 7.32 (d, *J* = 8.0 Hz, 1H), 7.21–7.16 (m, 1H), 7.09–7.02 (m, 1H), 7.01–6.94 (m, 2H), 6.08 (s, 2H), 4.66–4.56 (m, 1H), 3.29–3.14 (m, 2H). ^{13}C NMR (101 MHz, DMSO-d_6) δ 173.61, 165.40, 149.73, 147.21, 136.06, 127.87, 127.10, 123.55, 122.40, 120.91, 118.35, 118.07, 111.40, 110.43, 107.72, 107.35, 101.62, 53.71, 26.64. HRMS (ESI$^+$) m/z calculated for $C_{19}H_{16}N_2O_5$ [M + H] $^+$ 353.1132 and 353.1133.

(1H-Indole-3-Carbonyl)tryptophan (I-13)

Method C: White solid; yield: 85.3%. HPLC purity: 97.09%. m.p. 163.7–164.8 °C. ^{1}H NMR (400 MHz, DMSO-d_6) δ 12.53 (s, 1H), 11.56 (s, 1H), 10.81 (s, 1H), 8.12–8.06 (m, 1H), 8.02 (d, *J* = 7.9 Hz, 1H), 7.97 (d, *J* = 7.9 Hz, 1H), 7.67–7.58 (m, 1H), 7.41 (d, *J* = 8.0 Hz, 1H), 7.32 (d, *J* = 8.0 Hz, 1H), 7.24–7.18 (m, 1H), 7.18–7.10 (m, 1H), 7.09–7.02 (m, 2H), 7.02–6.94 (m, 1H), 4.77–4.64 (m, 1H), 3.29–3.12 (m, 2H). ^{13}C NMR (101 MHz, DMSO-d_6) δ 170.68, 150.58, 150.50, 136.04, 128.88, 128.67, 128.31, 123.63, 122.92, 120.66, 120.14, 119.93, 118.45, 118.11, 115.97, 111.19, 110.59, 54.29, 44.38, 27.49. HRMS (ESI$^+$) m/z calculated for $C_{20}H_{17}N_3O_3$ [M + H] $^+$ 348.1343, 348.1346.

(9H-Xanthene-9-Carbonyl)tryptophan (I-14)

Method C: White solid; yield: 83.6%. HPLC purity: 100%. m.p. 157.4–158.6 °C. ^{1}H NMR (400 MHz, DMSO-d_6) δ 10.82 (s, 1H), 8.49 (s, 1H), 7.56 (d, *J* = 7.8 Hz, 1H), 7.34 (d, *J* = 8.0 Hz, 1H), 7.30–7.15 (m, 3H), 7.14–6.99 (m, 5H), 6.99–6.92 (m, 1H), 6.90–6.82 (m, 1H), 6.81–6.74 (m, 1H), 5.01 (s, 1H), 4.34 (s, 1H), 3.13–2.99 (m, 2H). ^{13}C NMR (101 MHz, DMSO-d_6) δ 174.16, 164.52, 136.06, 128.24, 127.24, 126.01, 123.55, 121.84, 120.84, 120.36, 118.34, 111.80, 111.37, 110.49, 110.06, 52.89, 27.05. HRMS (ESI$^+$) m/z values calculated for $C_{25}H_{20}N_2O_4$ [M + H] $^+$ were 413.1496, 413.1498.

(1-Methyl-1H-Indole-3-Carbonyl)tryptophan (I-15)

Method C: White solid; yield: 83.7%. HPLC purity: 100%. m.p. 172.5–173.6 °C. ^{1}H NMR (400 MHz, DMSO-d_6) δ 12.59 (s, 1H), 10.81 (s, 1H), 8.07 (s, 1H), 8.03 (d, *J* = 7.9 Hz, 1H), 7.94 (d, *J* = 7.9 Hz, 1H), 7.65–7.56 (m, 1H), 7.51–7.44 (m, 1H), 7.36–7.28 (m, 1H), 7.24–7.16 (m, 2H), 7.15–7.09 (m, 1H), 7.08–7.02 (m, 1H), 7.02–6.95 (m, 1H), 4.76–4.66 (m, 1H), 3.82 (s, 3H), 3.30–3.12 (m, 2H). ^{13}C NMR (101 MHz, DMSO-d_6) δ 173.56, 167.97, 158.04, 136.55, 129.90, 127.73, 124.17, 121.61, 121.39, 118.88, 118.65, 115.10, 111.86, 110.11, 67.03, 53.18, 27.28. HRMS (ESI$^+$) m/z calculated for $C_{21}H_{19}N_3O_3$ [M + H] $^+$ 362.1499, found 362.1504.

Methyl (2-(p-Tolyloxy)acetyl)tryptophanate (II-1)

Method B: White solid, yield: 80.1%. yield HPLC purity: 100%. m.p. 113.3–114.2 °C. ^{1}H NMR (400 MHz, $CDCl_3$) δ 8.14 (s, 1H), 7.57 (d, *J* = 7.9 Hz, 1H), 7.38 (d, *J* = 8.1 Hz, 1H), 7.26–7.17 (m, 1H), 7.18–7.03 (m, 4H), 6.94–6.86 (m, 1H), 6.73–6.62 (m, 2H), 5.10–4.91 (m, 1H), 4.53–4.40 (m, 2H), 3.71 (s, 3H), 3.44–3.28 (m, 2H), 2.31 (s, 3H). ^{13}C NMR (101 MHz, $CDCl_3$) δ 171.90, 168.32, 155.11, 136.14, 131.37, 130.06, 127.48, 122.80, 122.27, 119.80, 118.51, 114.62,

111.27, 109.71, 67.48, 52.43, 52.42, 27.63, 20.50. HRMS (ESI^+) m/z calculated for $C_{21}H_{22}N_2O_4$ $[M + H]^+$ 367.1652, 367.1649.

Ethyl (2-(p-Tolyloxy)acetyl)tryptophanate (II-2)

Method B: White solid, yield: 85.4%. yield HPLC purity: 100%. m.p. 128.9–129.9 °C. ^1H NMR (400 MHz, $CDCl_3$) δ 8.18 (s, 1H), 7.59 (d, *J* = 7.9 Hz, 1H), 7.37 (d, *J* = 8.1 Hz, 1H), 7.25–7.14 (m, 2H), 7.14–7.03 (m, 3H), 6.96–6.87 (m, 1H), 6.76–6.63 (m, 2H), 5.07–4.91 (m, 1H), 4.53–4.39 (m, 2H), 4.24–4.05 (m, 2H), 3.46–3.27 (m, 2H), 2.31 (s, 3H), 1.29–1.14 (m, 3H). ^{13}C NMR (101 MHz, $CDCl_3$) δ 171.57, 168.50, 155.15, 136.27, 131.37, 130.07, 127.58, 123.07, 122.15, 119.65, 118.46, 114.68, 111.43, 109.51, 67.53, 61.64, 52.76, 27.69, 20.49, 14.09. HRMS (ESI^+) m/z calculated for $C_{22}H_{24}N_2O_4$ $[M + H]^+$ 381.1809, found 381.1809.

Isopropyl (2-(p-Tolyloxy)acetyl)tryptophanate (II-3)

Method B: White solid; yield: 81.9%. HPLC purity: 100%. m.p. 107.3–108.4 °C. ^1H NMR (400 MHz, $CDCl_3$) δ 8.17 (s, 1H), 7.60 (d, *J* = 7.9 Hz, 1H), 7.37 (d, *J* = 8.1 Hz, 1H), 7.24–7.18 (m, 1H), 7.18–7.14 (m, 1H), 7.14–7.08 (m, 1H), 7.07 (d, *J* = 8.7 Hz, 2H), 6.99–6.91 (m, 1H), 6.69 (d, *J* = 8.6 Hz, 2H), 5.07–4.88 (m, 2H), 4.53–4.37 (m, 2H), 3.41–3.27 (m, 2H), 2.31 (s, 3H), 1.21–1.14 (m, 6H). ^{13}C NMR (101 MHz, $CDCl_3$) δ 171.00, 168.23, 155.15, 136.08, 131.32, 130.05, 127.64, 122.70, 122.23, 119.72, 118.70, 114.62, 111.15, 109.99, 69.37, 67.53, 52.66, 27.72, 21.68, 20.50. HRMS (ESI^+) m/z calculated for $C_{23}H_{26}N_2O_4$ $[M + H]^+$ 395.1965, found 395.1962.

Benzyl (2-(p-Tolyloxy)acetyl)tryptophanate (II-4)

Method D: pale yellow solid, yield: 78.2%. HPLC purity: 100%. m.p. 133.1–134.6 °C. ^1H NMR (400 MHz, $CDCl_3$) δ 8.13 (s, 1H), 7.56–7.48 (m, 1H), 7.37–7.28 (m, 4H), 7.26–7.12 (m, 4H), 7.10–7.03 (m, 1H), 7.01 (d, *J* = 8.4 Hz, 2H), 6.69 (s, 1H), 6.62 (d, *J* = 8.4 Hz, 2H), 5.13–5.06 (m, 2H), 5.06–5.99 (m, 1H), 4.41 (s, 2H), 3.41–3.27 (m, 2H), 2.27 (s, 3H). ^{13}C NMR (101 MHz, $CDCl_3$) δ 171.30, 168.42, 155.11, 136.18, 135.26, 131.35, 130.08, 128.59, 128.42, 127.54, 123.02, 122.98, 122.20, 119.79, 118.52, 114.65, 111.33, 109.44, 67.51, 67.27, 52.69, 27.71, 20.48. HRMS (ESI^+) m/z calculated for $C_{27}H_{26}N_2O_4$ $[M + H]^+$ 443.1965, found 443.1963.

Cyclohexyl (2-(p-Tolyloxy)acetyl)tryptophanate (II-5)

Method D: pale yellow solid; yield: 81.4%. HPLC purity: 100%. m.p. 119.0–120.1 °C. ^1H NMR (400 MHz, $CDCl_3$) δ 8.24 (s, 1H), 7.57 (d, *J* = 7.9 Hz, 1H), 7.32 (d, *J* = 8.1 Hz, 1H), 7.16 (q, *J* = 7.3 Hz, 2H), 7.07 (t, *J* = 7.5 Hz, 1H), 7.02 (d, *J* = 8.3 Hz, 2H), 6.93–6.88 (m, 1H), 6.64 (d, *J* = 8.4 Hz, 2H), 5.03–4.90 (m, 1H), 4.82–4.66 (m, 1H), 4.50–4.30 (m, 2H), 3.42–3.23 (m, 2H), 2.27 (s, 3H), 1.72–1.22 (m, 10H). ^{13}C NMR (101 MHz, $CDCl_3$) δ 170.89, 168.28, 155.16, 136.15, 131.31, 130.03, 127.66, 122.82, 122.17, 119.67, 118.66, 114.63, 111.21, 109.88, 74.05, 67.55, 52.83, 31.33, 27.83, 25.27, 23.51, 20.46. HRMS (ESI^+) m/z calculated for $C_{26}H_{30}N_2O_4$ $[M + H]^+$ 435.2278, 435.2276.

Isopropyl (2-Phenoxyacetyl)tryptophanate (III-1)

Method B: White solid, 82.7% yield. HPLC purity: 100%. m.p. 144.2–145.3 °C. ^1H NMR (400 MHz, $CDCl_3$) δ 8.05 (s, 1H), 7.58 (d, *J* = 7.9 Hz, 1H), 7.34 (d, *J* = 8.1 Hz, 1H), 7.29–7.22 (m, 1H), 7.21–7.16 (m, 1H), 7.15–7.05 (m, 2H), 7.02–6.95 (m, 1H), 6.94–6.87 (m, 1H), 6.82–6.73 (m, 2H), 5.03–4.90 (m, 2H), 4.52–4.40 (m, 2H), 3.42–3.26 (m, 2H), 1.16 (t, *J* = 6.7 Hz, 6H). ^{13}C NMR (101 MHz, $CDCl_3$) δ 170.98, 168.03, 157.13, 136.05, 129.66, 127.61, 122.73, 122.24, 122.20, 119.73, 118.67, 114.74, 111.19, 109.90, 69.42, 67.22, 52.67, 27.67, 21.65. HRMS (ESI^+) m/z calculated for $C_{22}H_{24}N_2O_4$ $[M + H]^+$ 381.1809, found 381.1808.

Isopropyl (2-(4-Methoxyphenoxy)acetyl)tryptophanate (III-2)

Method B: White solid; yield: 74.5%. HPLC purity: 100%. m.p. 158.2–159.4 °C. ^1H NMR (400 MHz, $CDCl_3$) δ 8.07 (s, 1H), 7.50 (d, *J* = 7.9 Hz, 1H), 7.26 (d, *J* = 8.1 Hz, 1H), 7.15–7.08 (m, 1H), 7.08–7.03 (m, 1H), 7.03–6.97 (m, 1H), 6.88–6.81 (m, 1H), 6.69 (d, *J* = 9.1 Hz, 2H), 6.61 (d, *J* = 9.1 Hz, 2H), 4.96–4.82 (m, 2H), 4.39–4.25 (m, 2H), 3.68 (s, 3H), 3.31–3.22 (m, 2H), 1.13–1.05 (m, 6H). ^{13}C NMR (101 MHz, $CDCl_3$) δ 171.07, 168.43, 154.66, 151.41, 136.17, 127.65, 122.88, 122.15, 119.64, 118.60, 115.87, 114.73, 111.28, 109.76, 69.44, 68.21, 55.65, 52.78, 27.70, 21.72. HRMS (ESI^+) m/z calculated for $C_{23}H_{26}N_2O_5$ $[M + H]^+$ 411.1914, 411.1911.

Isopropyl (2-(4-Isopropylphenoxy)acetyl)tryptophanate (III-3)

Method B: White solid; yield: 77.2%. HPLC purity: 100%. m.p. 162.4–163.7 °C. ^{1}H NMR (400 MHz, $CDCl_3$) δ 8.05 (s, 1H), 7.58 (d, J = 7.9 Hz, 1H), 7.34 (d, J = 8.1 Hz, 1H), 7.12–7.16 (m, 1H), 7.16–7.04 (m, 4H), 6.95–6.87 (m, 1H), 6.71 (d, J = 8.6 Hz, 2H), 5.08–4.85 (m, 2H), 4.51–4.34 (m, 2H), 3.42–3.26 (m, 2H), 2.94–2.78 (m, 1H), 1.22 (d, J = 6.9 Hz, 6H), 1.14 (t, J = 6.4 Hz, 6H). ^{13}C NMR (101 MHz, $CDCl_3$) δ 171.07, 168.41, 155.35, 142.54, 136.22, 127.67, 127.44, 122.99, 122.14, 119.65, 118.62, 114.70, 111.34, 109.69, 69.45, 67.55, 52.86, 33.34, 27.76, 24.18, 21.67. HRMS (ESI^+) m/z calculated for $C_{25}H_{30}N_2O_4$ $[M + H]^+$ was 423.2278, found to be 423.2278.

Isopropyl (2-(4-Fluorophenoxy)acetyl)tryptophanate (III-4)

Method B: White solid; yield: 81.4%. HPLC purity: 100%. m.p. 185.1–186.4 °C. ^{1}H NMR (400 MHz, $CDCl_3$) δ 8.07 (s, 1H), 7.57 (d, J = 7.9 Hz, 1H), 7.35 (d, J = 8.1 Hz, 1H), 7.24–7.15 (m, 1H), 7.13–7.00 (m, 2H), 6.98–6.86 (m, 3H), 6.73–6.61 (m, 2H), 5.07–4.85 (m, 2H), 4.49–4.31 (m, 2H), 3.41–6.26 (m, 2H), 1.24–1.11 (m, 6H). ^{13}C NMR (101 MHz, $CDCl_3$) δ 171.00, 167.90, 157.87 (d, $J_{F\text{-}C}$ = 240.9 Hz), 153.30 (d, $J_{F\text{-}C}$ = 2.2 Hz), 136.11, 127.67, 122.73, 122.24, 119.72, 118.57, 116.01 (d, $J_{F\text{-}C}$ = 22.4 Hz), 115.94 (d, $J_{F\text{-}C}$ = 8.2 Hz), 111.25, 109.84, 69.48, 68.03, 52.80, 27.59, 21.67. HRMS (ESI^+) m/z calculated for $C_{22}H_{23}FN_2O_4$ $[M + H]^+$ 399.1715, 399.1712.

Isopropyl (2-(4-Chlorophenoxy)acetyl)tryptophanate (III-5)

Method B: White solid, 86.1% yield HPLC purity: 100%. m.p. 166.4–167.9 °C. ^{1}H NMR (400 MHz, $CDCl_3$) δ 8.12 (s, 1H), 7.56 (d, J = 7.9 Hz, 1H), 7.35 (d, J = 8.1 Hz, 1H), 7.23–7.14 (m, 3H), 7.11–7.05 (m, 1H), 7.05–7.98 (m, 1H), 6.95–6.87 (m, 1H), 6.69–6.58 (m, 2H), 5.04–4.96 (m, 1H), 4.96–4.89 (m, 1H), 4.47–4.30 (m, 2H), 3.44–3.22 (m, 2H), 1.24–1.09 (m, 6H). ^{13}C NMR (101 MHz, $CDCl_3$) δ 171.00, 167.70, 155.72, 136.13, 129.51, 127.64, 126.96, 122.77, 122.24, 119.73, 118.52, 116.05, 111.30, 109.73, 69.48, 67.56, 52.84, 27.54, 21.69. HRMS (ESI^+) m/z calculated for $C_{22}H_{23}ClN_2O_4$ $[M + H]^+$ 415.1419, found, 415.1419.

Isopropyl (2-(4-Bromophenoxy)acetyl)tryptophanate (III-6)

Method B: White solid; yield: 84.8%. HPLC purity: 95.74%. m.p. 181.5–182.4 °C. ^{1}H NMR (400 MHz, $CDCl_3$) δ 8.15 (s, 1H), 7.59 (d, J = 7.9 Hz, 1H), 7.38 (d, J = 8.1 Hz, 1H), 7.33 (d, J = 9.0 Hz, 2H), 7.25–7.18 (m, 1H), 7.14–7.07 (m, 1H), 7.07–6.99 (m, 1H), 6.98–6.89 (m, 1H), 6.61 (d, J = 9.0 Hz, 2H), 5.08–4.98 (m, 1H), 4.98–4.90 (m, 1H), 4.50–4.36 (m, 2H), 3.43–3.27 (m, 2H), 1.27–1.17 (m, 6H). ^{13}C NMR (101 MHz, $CDCl_3$) δ 170.95, 167.60, 156.12, 136.03, 132.38, 127.55, 122.70, 122.21, 119.69, 118.49, 116.45, 114.24, 111.26, 109.63, 69.48, 67.35, 52.75, 27.45, 21.69. HRMS (ESI^+) m/z values calculated for $C_{22}H_{23}BrN_2O_4$ $[M + H]^+$ 459.0914, 459.0913.

Isopropyl (2-(4-Formylphenoxy)acetyl)tryptophanate (III-7)

Method B: White solid; yield: 85.1%. HPLC purity: 100%. m.p. 174.6–175.9 °C. ^{1}H NMR (400 MHz, $CDCl_3$) δ 9.90 (s, 1H), 8.17 (s, 1H), 7.79 (d, J = 8.6 Hz, 2H), 7.58 (d, J = 7.9 Hz, 1H), 7.37 (d, J = 8.2 Hz, 1H), 7.26–7.17 (m, 1H), 7.12–7.06 (m, 1H), 7.06–6.99 (m, 1H), 6.99–6.94 (m, 1H), 6.83 (d, J = 8.7 Hz, 2H), 5.10–4.99 (m, 1H), 5.00–4.92 (m, 1H), 4.62–4.46 (m, 2H), 3.38 (s, 2H), 1.27–1.13 (m, 6H). ^{13}C NMR (101 MHz, $CDCl_3$) δ 189.73, 169.91, 166.05, 160.68, 135.12, 130.89, 129.83, 126.59, 121.82, 121.16, 118.66, 117.38, 113.97, 110.35, 108.49, 68.50, 66.12, 51.84, 26.40, 20.66. HRMS (ESI^+) m/z calculated for $C_{23}H_{24}N_2O_5$ $[M + H]^+$ 409.1758, 409.1755.

Isopropyl (2-(4-(Trifluoromethyl)phenoxy)acetyl)tryptophanate (III-8)

Method B: White solid; 79.3% yield. HPLC purity: 100%. m.p. 183.0–184.6 °C. ^{1}H NMR (400 MHz, $CDCl_3$) δ 8.04 (s, 1H), 7.56 (d, J = 8.0 Hz, 1H), 7.48 (d, J = 8.6 Hz, 2H), 7.35 (d, J = 8.2 Hz, 1H), 7.24–7.15 (m, 1H), 7.13–7.04 (m, 1H), 7.03–6.96 (m, 1H), 6.95–6.89 (m, 1H), 6.77 (d, J = 8.6 Hz, 2H), 5.05–4.97 (m, 1H), 4.97–4.89 (m, 1H), 4.55–4.41 (m, 2H), 3.44–3.23 (m, 2H), 1.24–1.11 (m, 6H). ^{13}C NMR (101 MHz, $CDCl_3$) δ 170.91, 167.23, 159.42, 136.10, 127.65, 127.06, 124.21 (q, $J_{F\text{-}C}$ = 32.8 Hz), 124.16 (q, $J_{F\text{-}C}$ = 272.3 Hz), 122.59, 122.33, 119.81, 118.51, 114.73, 111.26, 109.81, 69.49, 67.27, 52.85, 27.46, 21.68. HRMS (ESI^+) m/z calculated for $C_{23}H_{23}F_3N_2O_4$ $[M + H]^+$ 449.1683, found 449.1682.

Isopropyl (Furan-2-Carbonyl)tryptophanate (III-9)

Method B: White solid, yield: 78.1%. HPLC purity: 99.66%. m.p. 186.3–187.5 °C. ^{1}H NMR (600 MHz, $CDCl_3$) δ 8.38 (s, 1H), 7.58 (d, *J* = 7.9 Hz, 1H), 7.40–7.34 (m, 1H), 7.32 (d, *J* = 8.1 Hz, 1H), 7.19–7.12 (m, 1H), 7.12–7.03 (m, 2H), 7.03–6.99 (m, 1H), 6.96–6.85 (m, 1H), 6.48–6.39 (m, 1H), 5.11–5.02 (m, 1H), 5.02–4.90 (m, 1H), 3.55–3.24 (m, 2H), 1.25–1.01 (m, 6H). ^{13}C NMR (101 MHz, $CDCl_3$) δ 171.33, 157.92, 147.51, 144.23, 136.11, 127.67, 122.84, 122.15, 119.53, 118.81, 114.61, 112.08, 111.19, 110.04, 69.46, 52.78, 28.07, 21.66. HRMS (ESI^+) m/z calculated for $C_{19}H_{20}N_2O_4$ $[M + H]^+$ 341.1496, found 341.1494.

Isopropyl (Thiophene-2-Carbonyl)tryptophanate (III-10)

Method B: White solid; yield: 79.8%. HPLC purity: 99.71%. m.p. 176.1–177.8 °C. ^{1}H NMR (600 MHz, $CDCl_3$) δ 8.30 (s, 1H), 7.63–7.53 (m, 1H), 7.47–7.30 (m, 1H), 7.38–7.30 (m, 2H), 7.22–7.12 (m, 1H), 7.11–7.03 (m, 1H), 7.03–6.95 (m, 2H), 6.63–6.46 (m, 1H), 5.10–5.03 (m, 1H), 5.04–4.94 (m, 1H), 3.47–3.30 (m, 2H), 1.23–1.15 (m, 6H). ^{13}C NMR (101 MHz, $CDCl_3$) δ 171.40, 161.56, 138.43, 136.20, 130.32, 128.47, 127.76, 122.99, 122.18, 119.63, 118.72, 111.37, 109.85, 69.54, 53.63, 27.81, 21.74. HRMS (ESI^+) m/z values calculated for $C_{19}H_{20}N_2O_3S$ $[M + H]^+$ 357.1267, 357.1263.

Isopropyl Picolinoyltryptophanate (III-11)

Method B: White solid; yield: 81.6%. HPLC purity: 100%. m.p. 145.9–150.7 °C. ^{1}H NMR (600 MHz, $CDCl_3$) δ 8.63–8.47 (m, 1H), 8.46–8.37 (m, 1H), 8.34 (s, 1H), 8.18–7.95 (m, 1H), 7.76–7.63 (m, 1H), 7.58–7.45 (m, 1H), 7.39–7.14 (m, 2H), 7.13–7.02 (m, 1H), 7.01–6.81 (m, 2H), 5.12–4.96 (m, 1H), 4.94–4.76 (m, 1H), 3.46–3.14 (m, 2H), 1.17–0.93 (m, 6H). ^{13}C NMR (101 MHz, $CDCl_3$) δ 171.51, 164.20, 149.40, 148.24, 137.23, 136.23, 127.61, 126.27, 123.02, 122.17, 121.95, 119.31, 118.79, 111.26, 110.03, 69.29, 53.32, 28.23, 21.74. HRMS (ESI^+) m/z calculated for $C_{20}H_{21}N_3O_3$ $[M + H]^+$ 352.1656, found 352.1654.

Isopropyl (Thiazole-4-Carbonyl)tryptophanate (III-12)

Method B: White solid, 80.5% yield. HPLC purity: 100%. m.p. 150.6–151.8 °C. ^{1}H NMR (600 MHz, $CDCl_3$) δ 8.67 (s, 1H), 8.28 (s, 1H), 8.14 (s, 1H), 7.93 (d, *J* = 8.0 Hz, 1H), 7.60 (d, *J* = 7.9 Hz, 1H), 7.36–7.27 (m, 1H), 7.19–7.10 (m, 1H), 7.10–6.97 (m, 2H), 5.10–5.03 (m, 1H), 5.02–4.93 (m, 1H), 3.55–3.18 (m, 2H), 1.22–1.07 (m, 6H). ^{13}C NMR (101 MHz, $CDCl_3$) δ 171.34, 160.68, 152.80, 150.59, 136.22, 127.59, 123.54, 122.92, 122.02, 119.39, 118.75, 111.28, 109.97, 69.39, 53.18, 28.17, 21.73. HRMS (ESI^+) m/z values calculated for $C_{18}H_{19}N_3O_3S$ $[M + H]^+$ 358.1220, 358.1217.

Isopropyl (Benzo[B]thiophene-2-Carbonyl)tryptophanate (III-13)

Method B: White solid; yield: 81.9%. HPLC purity: 100%. m.p. 133.5–134.9 °C. ^{1}H NMR (600 MHz, $CDCl_3$) δ 8.50 (s, 1H), 7.76 (d, *J* = 8.0 Hz, 1H), 7.68 (d, *J* = 7.8 Hz, 1H), 7.64–7.56 (m, 1H), 7.52 (s, 1H), 7.41–7.28 (m, 3H), 7.21–7.11 (m, 1H), 7.10–7.03 (m, 1H), 7.02–6.94 (m, 1H), 6.85–6.70 (m, 1H), 5.14–5.05 (m, 1H), 5.04–4.93 (m, 1H), 3.50–3.32 (m, 2H), 1.24–1.11 (m, 6H). ^{13}C NMR (101 MHz, $CDCl_3$) δ 171.28, 161.93, 141.03, 139.03, 138.04, 136.19, 127.80, 126.38, 125.51, 125.10, 124.86, 123.06, 122.67, 122.24, 119.71, 118.79, 111.36, 109.88, 69.61, 53.82, 27.77, 21.79. HRMS (ESI^+) m/z values calculated for $C_{23}H_{22}N_2O_3S$ $[M + H]^+$ 407.1424, 407.1420.

Isopropyl (Benzo[D][1,3]dioxole-5-Carbonyl)tryptophanate (III-14)

Method B: White solid; yield: 82.4%. HPLC purity: 99.71%. m.p. 144.8–145.7 °C. ^{1}H NMR (600 MHz, $CDCl_3$) δ 8.38 (s, 1H), 7.56 (d, *J* = 7.9 Hz, 1H), 7.32 (d, *J* = 8.1 Hz, 1H), 7.22–7.13 (m, 3H), 7.10–7.02 (m, 1H), 7.01–6.94 (m, 1H), 6.80–6.66 (m, 1H), 6.63–6.52 (m, 1H), 5.97 (s, 2H), 5.09–5.03 (m, 1H), 5.03–4.92 (m, 1H), 3.50–3.25 (m, 2H), 1.23–1.13 (m, 6H). ^{13}C NMR (101 MHz, $CDCl_3$) δ 171.55, 166.16, 150.40, 147.86, 136.03, 128.17, 127.78, 122.74, 122.23, 121.78, 119.63, 118.85, 111.19, 110.22, 107.92, 107.67, 101.64, 69.38, 53.61, 27.66, 21.72. HRMS (ESI^+) m/z calculated for $C_{22}H_{22}N_2O_5$ $[M + H]^+$ 395.1601, found 395.1601.

Isopropyl (2,3-Dihydrobenzo[B][1,4]dioxine-2-Carbonyl)tryptophanate (III-15)

Method B: White solid; 79.1% yield HPLC purity: 100%. m.p. 137.6–138.7 °C. ^{1}H NMR (600 MHz, $CDCl_3$) δ 8.42–8.04 (m, 1H), 7.68–7.45 (m, 1H), 7.39–7.25 (m, 1H), 7.23–7.00 (m, 3H), 6.99–6.76 (m, 4H), 6.75–6.59 (m, 1H), 5.00–4.91 (m, 1H), 4.90–4.83 (m, 1H), 4.66–4.57 (m, 1H), 4.51–4.30 (m, 1H), 4.16–4.02 (m, 1H), 3.40–3.20 (m, 2H), 1.21–1.07

(m, 6H). ^{13}C NMR (101 MHz, $CDCl_3$) δ 170.87 and 170.60, 166.96 and 166.89, 143.34 and 143.12, 141.67 and 141.52, 136.11 and 135.91, 127.68 and 127.50, 122.73 and 122.70, 122.38 and 122.28, 122.23 and 122.21, 121.93 and 121.82, 119.82 and 119.60, 118.73 and 118.64, 117.61 and 117.52, 117.37 and 117.21, 111.26 and 111.11, 109.93 and 109.63, 73.16 and 73.06, 69.65 and 69.40, 65.19 and 64.87, 52.98 and 52.81, 27.57 and 27.45, 21.71 and 21.66. HRMS (ESI^+) m/z calculated for $C_{23}H_{24}N_2O_5$ $[M + H]^+$ 409.1758, 409.1755.

Isopropyl (1H-Indole-3-Carbonyl)tryptophanate (III-16)

Method B: Gray solid, yield: 78.2%. HPLC purity: 100%. m.p. 154.9–156.1 °C. ^{1}H NMR (600 MHz, DMSO-d_6) δ 11.60 (s, 1H), 10.85 (s, 1H), 8.18–8.09 (m, 2H), 8.05 (d, J = 8.0 Hz, 1H), 7.66–7.53 (m, 1H), 7.43 (d, J = 8.1 Hz, 1H), 7.35 (d, J = 8.1 Hz, 1H), 7.27–7.19 (m, 1H), 7.15 (t, J = 8.0 Hz, 1H), 7.13–7.04 (m, 2H), 7.04–6.96 (m, 1H), 4.93–4.83 (m, 1H), 4.75–4.66 (m, 1H), 3.32–3.15 (m, 2H), 1.21–1.03 (m, 6H). ^{13}C NMR (101 MHz, DMSO-d_6) δ 172.19, 164.52, 136.03, 128.29, 127.16, 126.03, 123.64, 123.57, 121.85, 120.86, 120.36, 118.34, 118.05, 111.78, 111.39, 109.89, 67.66, 53.20, 27.08, 26.32, 21.55, 21.28. HRMS (ESI^+) m/z calculated for $C_{23}H_{23}N_3O_3$ $[M + H]^+$ 390.1812, found 390.1810.

Isopropyl (Quinoline-3-Carbonyl)tryptophanate (III-17)

Method B: White solid, yield: 84.0%. HPLC purity: 100%. m.p. 157.7–158.8 °C. ^{1}H NMR (600 MHz, $CDCl_3$) δ 9.15 (s, 1H), 8.52 (s, 1H), 8.32 (s, 1H), 8.18–8.01 (m, 1H), 7.86–7.69 (m, 2H), 7.65–7.47 (m, 2H), 7.40–7.28 (m, 1H), 7.23–7.13 (m, 1H), 7.12–7.04 (m, 1H), 7.04–7.00 (m, 1H), 6.98–6.83 (m, 1H), 5.21–5.11 (m, 1H), 5.11–4.98 (m, 1H), 3.58–3.35 (m, 2H), 1.32–1.20 (m, 6H). ^{13}C NMR (101 MHz, $CDCl_3$) δ 171.40, 165.28, 149.16, 148.30, 136.20, 135.61, 131.28, 129.21, 128.76, 127.43, 126.74, 126.51, 122.93, 122.86, 122.36, 119.77, 118.60, 111.43, 109.90, 69.68, 53.89, 27.55, 21.82. HRMS (ESI^+) m/z calculated for $C_{24}H_{23}N_3O_3$ $[M + H]^+$ 402.1812; found: 402.1812.

Isopropyl (Quinoline-2-Carbonyl)tryptophanate (III-18)

Method B: White solid; yield: 82.9%. HPLC purity: 100%. m.p. 166.4–167.5 °C. ^{1}H NMR (400 MHz, $CDCl_3$) δ 8.82 (d, J = 8.2 Hz, 1H), 8.37 (s, 1H), 8.28–8.17 (m, 2H), 7.98 (d, J = 8.5 Hz, 1H), 7.81 (d, J = 8.1 Hz, 1H), 7.75–7.63 (m, 2H), 7.56 (t, J = 7.5 Hz, 1H), 7.31 (d, J = 8.1 Hz, 1H), 7.15 (t, J = 7.5 Hz, 1H), 7.11–7.01 (m, 2H), 5.18–5.07 (m, 1H), 5.07–4.93 (m, 1H), 3.51–3.39 (m, 2H), 1.22–1.09 (m, 6H). ^{13}C NMR (101 MHz, $CDCl_3$) δ 171.52, 164.36, 149.20, 146.50, 137.36, 136.23, 129.95, 129.31, 127.94, 127.70, 127.61, 123.03, 122.96, 122.05, 119.49, 118.93, 118.68, 111.25, 110.20, 69.27, 53.58, 28.19, 21.61. HRMS (ESI^+) m/z values calculated for $C_{24}H_{23}N_3O_3$ $[M + H]^+$ 402.1812, 402.1810.

Isopropyl (Quinoline-6-Carbonyl)tryptophanate (III-19)

Method B: pale yellow solid, yield: 78.3%. HPLC purity: 100%. m.p. 161.2–162.4 °C. ^{1}H NMR (600 MHz, DMSO-d_6) δ 10.86 (s, 1H), 9.09–9.01 (m, 1H), 9.01–8.95 (m, 1H), 8.54–8.49 (m, 1H), 8.49–8.43 (m, 1H), 8.21–8.12 (m, 1H), 8.12–8.04 (m, 1H), 7.67–7.53 (m, 2H), 7.38–7.31 (m, 1H), 7.30–7.21 (m, 1H), 7.12–7.04 (m, 1H), 7.03–7.96 (m, 1H), 5.00–4.82 (m, 1H), 4.79–4.59 (m, 1H), 3.32–3.23 (m, 2H), 1.31–0.97 (m, 6H). ^{13}C NMR (101 MHz, DMSO-d_6) δ 171.51, 166.04, 152.10, 148.68, 137.03, 136.12, 131.61, 128.94, 128.22, 127.77, 127.13, 127.00, 123.71, 122.16, 120.96, 118.39, 118.06, 111.43, 109.88, 67.92, 54.27, 26.73, 21.56, 21.30. HRMS (ESI^+) m/z values calculated for $C_{24}H_{23}N_3O_3$ $[M + H]^+$ 402.1812, 402.1810.

Isopropyl (Quinoxaline-2-Carbonyl)tryptophanate (III-20)

Method B: Yellow solid; yield: 77.5%. HPLC purity: 100%. m.p. 159.4–160.2 °C. ^{1}H NMR (400 MHz, DMSO-d_6) δ 10.92 (s, 1H), 9.45 (s, 1H), 9.05–8.93 (m, 1H), 8.27–8.10 (m, 2H), 8.06–7.91 (m, 2H), 7.60 (d, J = 7.9 Hz, 1H), 7.36 (d, J = 8.1 Hz, 1H), 7.29–7.18 (m, 1H), 7.14–7.03 (m, 1H), 7.03–6.92 (m, 1H), 4.99–4.89 (m, 1H), 4.88–4.80 (m, 1H), 3.47–3.39 (m, 2H), 1.23–1.11 (m, 6H). ^{13}C NMR (101 MHz, DMSO-d_6) δ 170.75, 162.84, 143.43, 143.05, 139.61, 136.12, 132.06, 131.35, 129.38, 129.06, 127.21, 123.92, 123.85, 121.01, 118.42, 118.14, 111.44, 109.08, 68.46, 53.52, 26.72, 21.31. HRMS (ESI^+) m/z calculated for $C_{23}H_{22}N_4O_3$ $[M + H]^+$ 403.1765, 403.1766.

Isopropyl (Quinoxaline-6-Carbonyl)tryptophanate (III-21)

Method B: White solid; yield: 74.9%. HPLC purity: 100%. m.p. 176.4–177.5 °C. ^{1}H NMR (600 MHz, DMSO-d_6) δ 10.87 (s, 1H), 9.23 (d, J = 7.4 Hz, 1H), 9.10–8.92 (m, 2H), 8.70–8.55 (m, 1H), 8.24 (dd, J = 8.7, 1.9 Hz, 1H), 8.18 (d, J =

8.7 Hz, 1H), 7.61 (d, J = 7.9 Hz, 1H), 7.35 (d, J = 8.1 Hz, 1H), 7.27 (d, J = 2.1 Hz, 1H), 7.13–7.03 (m, 1H), 7.03–6.95 (m, 1H), 4.96–4.87 (m, 1H), 4.77–4.66 (m, 1H), 3.34–3.25 (m, 2H), 1.26–1.03 (m, 6H). ^{13}C NMR (101 MHz, DMSO-d_6) δ 171.38, 165.54, 147.02, 146.63, 143.38, 141.49, 136.12, 134.89, 129.31, 128.59, 127.08, 123.73, 123.66, 120.95, 118.39, 118.02, 111.42, 109.89, 67.97, 54.31, 26.62, 21.27. HRMS (ESI$^+$) m/z calculated for $C_{23}H_{22}N_4O_3$ [M + H] $^+$ 403.1765, 403.1763.

Isopropyl (9H-Xanthene-9-Carbonyl)tryptophanate (III-22)

Method B: White solid, yield: 80.7%. yield HPLC purity: 100%. m.p. 154.8–155.7 °C. ^{1}H NMR (400 MHz, $CDCl_3$) δ 7.92 (s, 1H), 7.44–7.37 (m, 1H), 7.31–7.25 (m, 3H), 7.24–7.19 (m, 2H), 7.19–7.13 (m, 1H), 7.13–7.09 (m, 1H), 7.08–6.95 (m, 4H), 6.52–6.44 (m, 1H), 5.94–5.77 (m, 1H), 4.89–4.75 (m, 2H), 4.76–4.64 (m, 1H), 3.21–3.08 (m, 2H), 1.05–0.92 (m, 6H). ^{13}C NMR (101 MHz, DMSO-d_6) δ 171.05, 150.56, 136.15, 128.53, 127.16, 123.84, 123.77, 123.05, 120.96, 119.79, 119.57, 118.40, 118.10, 116.25, 111.40, 109.43, 68.03, 53.40, 44.23, 26.99, 21.26. HRMS (ESI$^+$) m/z calculated for $C_{28}H_{26}N_2O_4$ [M + H] $^+$ 455.1965, found 455.1965.

MD Simulation

Gromacs2023 was selected as the kinetic simulation software, and Amber99sb-ildn was selected as the protein and small molecule force field. TIP3P water was added to the system using the TIP3P model to establish a water box with a size of 10*10*10 nm3 (the edge of the water box was at least 1.2 nm away from the protein edge), and an automatic ion equilibrium system was added.

Particle-mesh Ewald (PME) was used to handle electrostatic interactions, and energy minimization was used for the maximum number of steps (50,000 steps) using the steepest descent method. The cut-off distance of the Coulomb force and the van der Waals radius were both 1 nm, and the canonical system (NVT) and the isothermal and isobaric system (NPT) were adopted to balance the system. Then, the MD simulation of 100ns was performed at room temperature and pressure. The non-bonding interaction cut-off value was set to 10 Å. The simulated temperature was controlled at 300 K using the V-rescale temperature coupling method and the pressure at 1 bar using the Berendsen method.

The built-in analysis module of Gromacs2023 was used to analyze the simulated trajectories. RMSD (root mean square deviation) was used to observe the overall conformational change of the protein relative to the initial structure during the simulation. Rg (radius of gyration) was used to evaluate the tightness of the architecture. RMSF (root mean square function) was used to observe the structural fluctuations of local amino acid residue sites in the system during the simulation process. Gmx_MMPBSA was used to calculate the binding free energy. Binding free energy calculations were performed by subtracting the free energies of the isolated receptor (ΔGreceptor) and ligand (ΔGligand) from that of the bound complex (ΔGcomplex), as expressed by the fundamental equation ΔGbind = ΔGcomplex - ΔGreceptor - ΔGligand.

Cell Lines

HEK293 cells were obtained from the Cell Bank of the Chinese Academy of Sciences (Shanghai, China). Cells were grown in corresponding medium containing 10% fetal bovine serum (FBS) at 37 °C and 5% CO_2.

$P2Y_{14}R$ Inhibitory Activity Screening

HEK293-h$P2Y_{14}R$ cells were seeded in each well of a 96-well plate. Cells were treated with the tested compounds and then stimulated with the intracellular cAMP inducer, forskolin (TargetMol, Shanghai, China). cAMP levels were detected using a cAMP-Glo Assay Kit (Promega, Madison, Wisconsin, USA). This is a common method used to evaluate adenylate cyclase activity, which is closely related to $P2Y_{14}R$ function.[10–12] Prism was used to analyze the data, and the curve-fitting equation was "log(antagonist) vs response-variable slope".

Selectivity of II-3 on $P2Y_1$, $P2Y_2$, $P2Y_6$, and $P2Y_{12}$ Receptors

The selectivity of **II-3** for different P2Y receptors was determined using an IP3 production assay ($P2Y_{1,2,4,6}R$) or cAMP production assay ($P2Y_{12}R$). HEK293 cells stably expressing h$P2Y_1R$ ($P2Y_1R$-HEK293 cells), h$P2Y_2R$ ($P2Y_2R$-HEK293

cells), hP2Y$_4$R (P2Y$_4$R-HEK293 cells), hP2Y$_6$R (P2Y$_6$R-HEK293 cells), or hP2Y$_{12}$R (P2Y$_{12}$R-HEK293 cells) were grown to 85–90% confluence prior to assays in DMEM supplemented with 10% FBS. The cells were treatment for 0.5 h with various concentrations of **II-3** and then stimulated with the physiological ligand at a concentration that corresponds to its EC_{50}:500 nM ADP for P2Y$_1$R, 500 nM UTP for P2Y$_2$R and P2Y$_4$R, 750 nM UDP for P2Y$_6$R, and 320 nM 2-MeSADP for the P2Y$_{12}$R receptor. IP3 and cAMP levels were then detected using an IP3 (Inositol Triphosphate) ELISA Kit (Elabscience, Wuhan, China) or cAMP-GloTM Assay (Promega, WI, USA).

Cytochrome P450 Inhibition

To further explore the druggability of II-3, We conducted Cytochrome P450 Inhibition test. Human liver microsomes are a well-established in vitro model that mimics the metabolic environment of the human liver. They contain the major drug-metabolizing enzymes, making them suitable for predicting the metabolic fate of II-3 in humans. Human liver microsomes (Sigma-Aldrich, St. Louis, America) were stored in a −80 °C freezer. All samples were incubated in a 37 °C water bath. A total of 98 μL of microsome working solution (0.5 mg/kg) and 2 μL of the test product were added and incubated in a water bath for 10 min. Different substrates were added to the solution containing each CYP enzyme. CYP1A2 substrate: Phenacetin (75 μM). CYP2C9 substrate: diclofenac (10 μM). CYP2C19 substrate: toin (10 μM). CYP2D6 substrate: Dextromethorphan (10 μM). CYP3A4 substrate: midazolam (2 μM). After 30 min of incubation, metabolites were analyzed by LC/MS.

Microsomal Stability Assay

To further explore the druggability of II-3, liver microsomal incubation was conducted in triplicate. The adaptability of this method refers to its suitability and effectiveness in assessing the metabolic stability and potential drug interactions of II-3. Test **II-3** (20 mM) was preincubated with human liver microsomes (0.2 mg/mL) and cofactor NADPH (1 mM) in a total volume of 400 mL of potassium phosphate buffer (0.5 mM NADP+, 5 mM $MgCl_2$, 10 mM glucose 6-phosphate, and 1 unit/mL G6PDH) at 37 °C. After 5 min of pre-incubation, 50 mL of the sample mixture was collected at 0, 5, 10, 15, 30, and 45 min and terminated with 100 μL EtOAc containing the internal standard. The resulting mixture was centrifuged and the supernatant was subjected to LC–MS analysis. The natural log of the amount of remaining parent compound was plotted against time to calculate the rate of disappearance and half-life of the tested compound.

hERG K+ Channel Inhibition Assay

To further explore the druggability of II-3, Whole-cell recordings were performed by using an automated QPatch system (Sophion, Denmark). hERG-HEK293 cells were harvested and adjusted to 2–5 million/mL for the automated QPatch 16X experiments. The cells were voltage-clamped at a holding potential of −80 mV. The hERG current was activated by depolarizing at +20 mV for 5 s, after which the current was returned to −50 mV for 5 s to remove inactivation and observe the deactivating tail current. The maximum tail current is used to determine the amplitude of the hERG current. It is crucial because hERG inhibition can lead to potentially fatal cardiac arrhythmias. Testing for hERG liability is a standard safety assessment in drug development.

Pharmacokinetic Studies

To further explore the druggability of II-3, Pharmacokinetic studies were performed using male SD mice aged 6–8 weeks (200–220 g, n = 3 per group) in compliance with the Guide for the Care and Use of Laboratory Animals. Compound II-3 was prepared as a solution containing 5% DMSO and 95% sodium carboxymethyl cellulose (CMC). The intragastric administration group was administered 20 mg/kg and the tail vein injection group was administered 10 mg/kg. The collection time points after the administration of the test compounds were 0.25, 0.5, 1, 2, 4, 8, and 24 h before and after the administration of the test substances. Blood samples were collected and placed on ice, and plasma was centrifuged for separation within 1 h. The blood sample was centrifuged to obtain the plasma, which was stored at −80 °C before analysis. The ratio of the sample peak area to the internal standard peak area was used as an indicator, and pharmacokinetic parameters were analyzed using the Phoenix WinNonlin v6.3 noncompartment model. The experimental design involving oral and intravenous administration allows for the evaluation of the pharmacokinetic characteristics of II-3

under different routes of administration. This helps to understand its bioavailability and distribution, providing crucial pharmacokinetic data to support the drug development of II-3.

LPS-Induced ALI in Mice

C57BL/6 mice (male; 6–8 weeks) were purchased from Skobes Biotechnology Co., Ltd. (Henan, China) and kept in a quarantine room for one week to adapt to the environment. This procedure was in strict compliance with the protocol endorsed by the National Institutional Animal Care and Ethical Committee at Zhengzhou University. To further explore the pro-inflammatory mechanisms of $P2Y_{14}R$ in ALI. Mice were divided into five groups: control, LPS, II-3-treated (2 and 6 mg/kg), and DXMS-treated (2 mg/kg). Each group consisted of six mice. Compound **II-3** (2 and 6 mg/kg) and dexmedetomidine (2 mg/kg) were administered by gavage once daily for seven consecutive days. One hour after the last administration, acute lung injury models were established in all groups, except for the control group. After anesthetization, endotoxin (8 mg/kg) was injected intratracheally. The mice were then placed in a vertical position and shaken slowly for 1 min to ensure that the drug was evenly distributed in the lungs. The wound was sutured and LPS (10 mg/kg) was injected intraperitoneally. The control and LPS groups were administered 0.5% CMC via oral gavage. Twenty-four hours after LPS administration, the animals were euthanized by isoflurane inhalation, after which BALF and lung tissue samples were collected.

Histopathologic Examination of Lung Tissues

For histopathological analysis, the superior lobe of the right lung tissue was first excised and fixed in a 4% paraformaldehyde solution for 24 h at 4 °C to preserve tissue structure. After fixation, the tissues were washed in phosphate-buffered saline (PBS) to remove any residual fixative. The tissues were then subjected to a graded series of ethanol solutions for dehydration, starting with 70% ethanol and increasing to 100%. After dehydration, tissues were cleared in xylene and infiltrated with molten paraffin wax. Paraffin-embedded tissues were oriented and sectioned at a thickness of 5 μm using a microtome.

The resulting sections were mounted onto glass slides, and any excess wax was removed by baking the slides at 60 °C for 1 h. Sections were deparaffinized in xylene and rehydrated using a descending alcohol series in water. For staining, the sections were immersed in hematoxylin for 5 min to stain the nuclei, followed by a quick rinse in running tap water. Afterward, the sections were stained with eosin for 1–2 minutes to color the cytoplasm and the extracellular matrix. The slides were then dehydrated again using an ethanol series, cleared in xylene, and coverslipped with resinous mounting medium.

Finally, the stained sections were examined under a Nikon Ni-U microscope (Nikon, Tokyo, Japan) to visualize and assess histopathological changes, including cellular infiltration, tissue damage, and structural alterations, indicative of inflammation.

Immunofluorescence

We utilized the TSA-based multiple immunofluorescencemethod. After fixing and permeabilizing the lung tissue sections, we blocked nonspecific-binding sites with blockingbuffer. We then incubated the sections with a cocktail of primary antibodies specific for the proteins of interest, including F4/80 (Abways, Beijing, China) and $P2Y_{14}R$ (Abclone, Wuhan, China). Following a thorough wash to remove unbound primary antibodies, we applied fluorophore-conjugated secondary antibodies and proceeded with the TSA amplification step. This involved the use of tyramide conjugated to a fluorophore, which was selectively bound to the secondary antibodies through horseradish peroxidase-catalyzed reactions. After quenching the reaction and washing away excess reagents, the slides were mounted with a fluorescence-preserving medium and analyzed using a confocal microscope.

Analysis of BALF

After euthanasia, the BALF was collected by inserting a retention needle into the trachea and securing it with a surgical suture to ensure a closed airway. To standardize the volume of each lavage, 1 mL physiological saline was instilled into the lungs. The chest cavity was gently massaged to facilitate saline distribution and promote equilibration with the

bronchoalveolar lining fluid. Saline, containing cellular and soluble components from the lungs, was carefully aspirated into a collection tube. The collected BALF samples were centrifuged at 1000 rpm for 10 min at 4 °C. The supernatant of the samples was collected and used to assess protein and cytokine concentrations.

ELISA

The protein levels of cytokines, including IL1β (R&D Systems, Minneapolis, MN, USA), IL-6 (Boster, Wuhan, China), and TNF-α (Boster, Wuhan, China) in the BALF supernatant, and MPO (Thermo Fisher, Waltham, MA) in the lung tissue were measured using enzyme-linked immunosorbent assay (ELISA) kits according to the manufacturer's instructions.

Statistical Analysis

Statistical analyses were performed using GraphPad Prism version 8.0. Data are shown as the mean ± standard deviation from at least three independent experiments. For multiple comparisons, One-way analysis of variance (ANOVA) was performed after the assessment of normal distribution and homogeneity of variance test. Differences were considered statistically significant at $p < 0.05$.

Results and Discussion

Molecule Design

In 2020, Hu et al reported a series of hit compounds of $P2Y_{14}R$ with novel scaffolds using a Glide-docking-based virtual screening (VS) strategy. Compound **7** is one of the hit compounds, which has exhibited moderate antagonistic activity with IC_{50} value of 35.4 nM.[29]

In this study, the protein structure used for molecular docking is $hP2Y_{14}R$ protein structure reported by the Jacobson group.[26] As shown in Figure 6A and B, the binding mode and interactions between compound **7** and $hP2Y_{14}R$ were displayed, which proved the key effects of the antagonistic activity of compound **7**: (1) the indole moiety directed to the extracellular solvent area and formed π-H interactions with Lys160 and Cys161, H-bonding with Gln249, (2) the 4-methylbenzene moiety entered into the hydrophobic pocket and interacted with Tyr91 via π–π interactions, Arg242 and Val88 via π-H interactions, and (3) the carboxylic acid moiety did not form any interactions with the surrounding residues, and there was a part of the unoccupied space below it. These results suggest that the above three parts can be modified to improve the antagonistic activity and druggability. This year, our group reported an article on modifying the indole moiety of compound **7**.[34] Therefore, the indole moiety was not considered in the process of structural

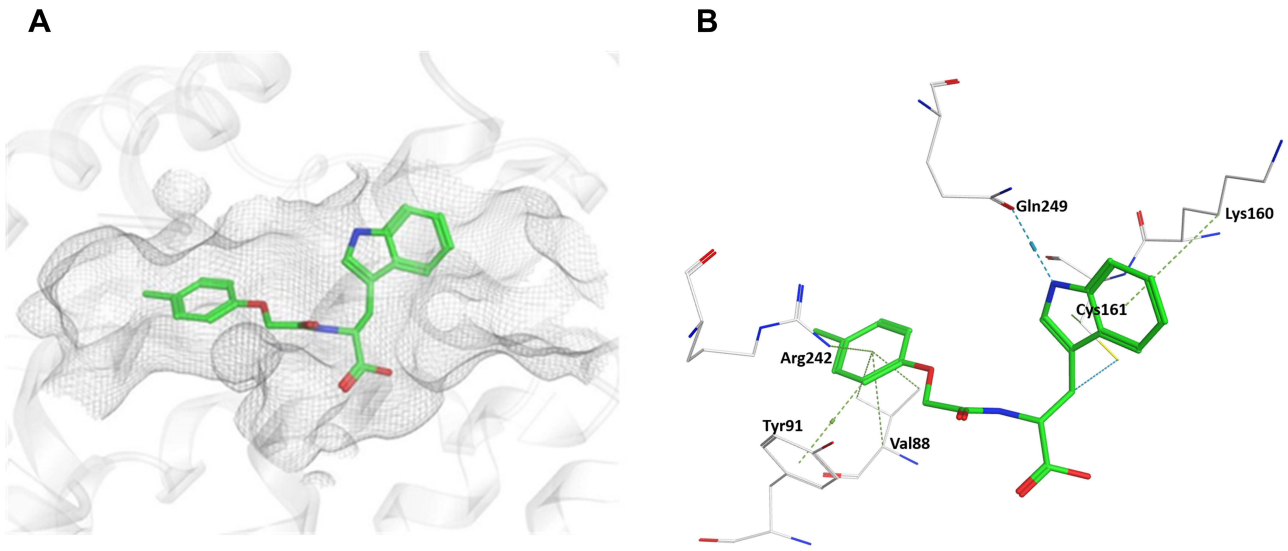

Figure 6 (**A**) The binding site of hit compound **7** in the active pocket of $hP2Y_{14}R$. (**B**) The interactions between hit compound **7** and the residues of $hP2Y_{14}R$.

https://doi.org/10.2147/DDDT.S497291

modification. Most currently reported $P2Y_{14}R$ antagonists contain amide bonds, and Figure 6 shows that the amide bond of compound **7** forms H-bonds with Lys66 of $hP2Y_{14}R$. Thus, the amide bond remains in the novel antagonists as a tool to connect different pharmacophores.

The overlap modes of **PPTN** and **7** in $hP2Y_{14}R$ are shown in Figure 7. It can be seen that the carboxylic acid part of compound **7** had no interaction with $hP2Y_{14}R$, but the carboxylic acid part of **PPTN** formed H-bonding with Lys66. Therefore, modifying the carboxylic acid portion of **7** to interact with $P2Y_{14}R$ and enhance its antagonistic activity of the compound **7** was used in this study. Based on these findings, three series of novel $P2Y_{14}R$ antagonists were designed. In series **I**, the methyl groups in benzene and p-methylphenoxymethylene groups were optimized based on compound **7**, hoping that the compound could penetrate deeper into the pocket, bind to the receptor more firmly, and achieve the effect of increase antagonistic activity. Considering that the 4-methylbenzene moiety entered the hydrophobic pocket, which has been reported by different groups,[27–29] the bioactivity of the orthotopic substituents on the benzene ring is relatively good relative to the ortho- and meta-substituents. Therefore, in the process of modifying the substituents on the benzene ring, we mainly changed the type of para-substituents. We also selected aromatic heterocycles to replace the p-methylphenoxymethylene group and directly connect them to the amide bond to further explore whether aromatic heterocycles have better biological activity than benzene rings. After Series 1 was explored, some of the active substituents were retained. In series **II**, the use of an ester pro-drug to cap the acid moiety was recognized as an effective method to eliminate zwitterionic characteristics and improve the oral biological activity.[24] Thus, ester groups of different sizes are introduced here. In series **III**, after selecting the optimal ester group in series **II**, the methyl groups in benzene and p-methylphenoxymethylene groups were optimized based on series **I**.

In summary, by improving the structure–activity relationship through the design of the three series of antagonists, we expect to find compounds with better binding ability and druggability with $P2Y_{14}R$ and simultaneously provide a theoretical basis for the discovery and optimal design of other skeletal types of $P2Y_{14}R$ antagonists.

Chemistry

Series **I** was synthesized from **26**, which was reacted with different commercially available 2-(4-substitutedphenoxy) acetic acids or aryl carboxylic acids to obtain ester intermediates, which yielded target compounds **I-1~I-15**, as shown in Scheme 1.

In Series **II**, the carboxyl group of tryptophan was activated by thionyl chloride and reacted with methanol, ethanol, and isopropanol to obtain intermediates **26~28**. The reaction of the intermediates with 2-(p-tolyloxy)acetic acid, using EDCI and HOBt as condensation agents, provided compounds **II-1~II-3**. In addition, owing to the low yields of benzyl alcohol and cyclohexanol, the conventional esterification method was not applicable. Thus, compound **II-1** was first

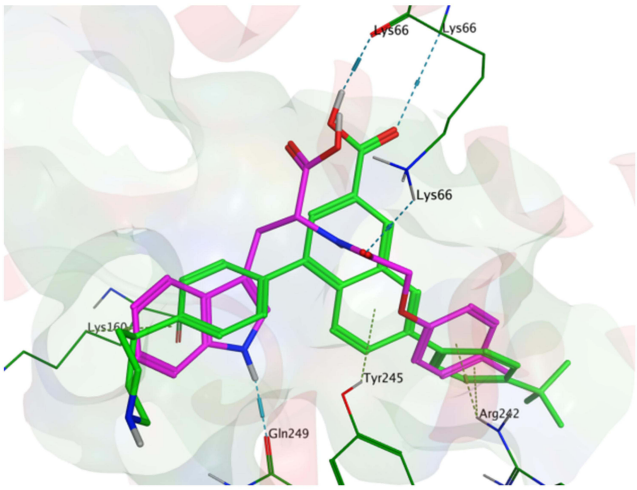

Figure 7 The overlap mode of **PPTN** and hit compound **7** in $hP2Y_{14}R$.

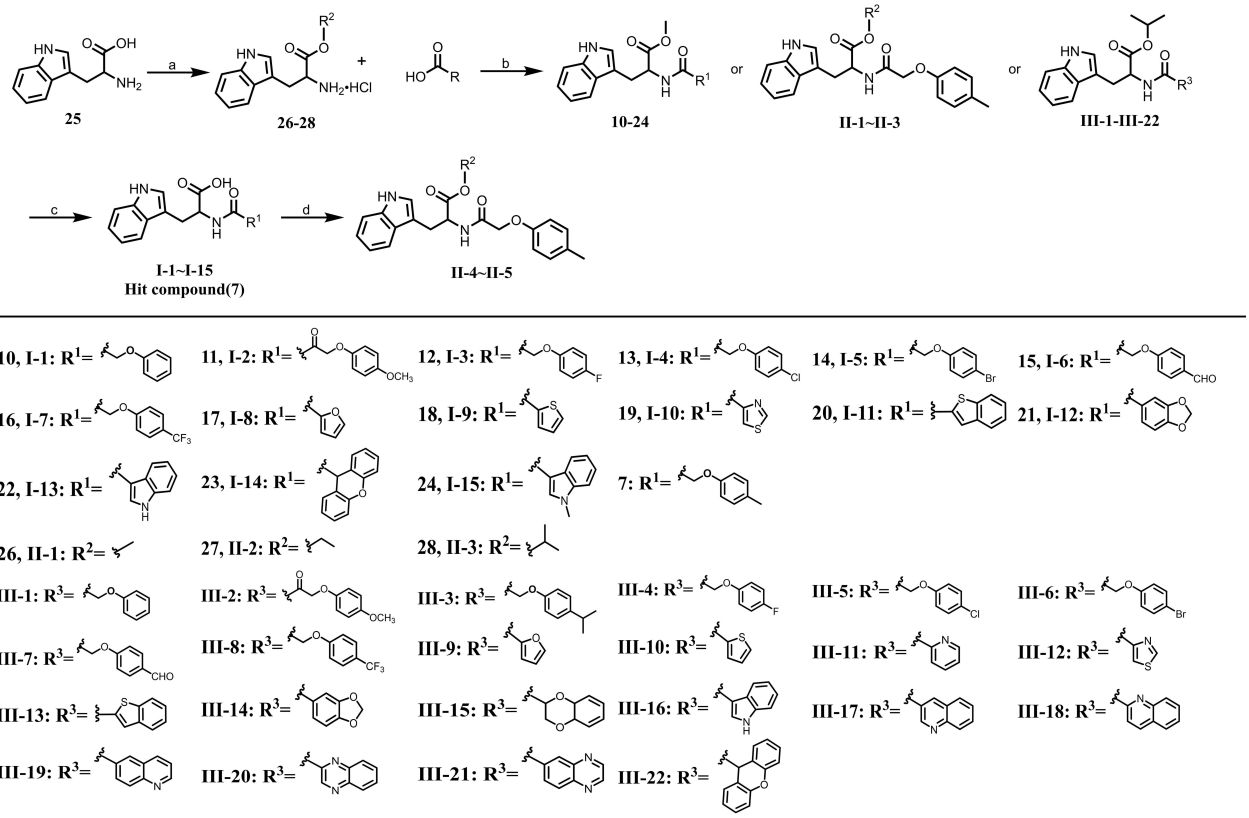

Scheme 1 Access to target compounds with diverse R functionality. R^1: Substituting Group of **I** Series Compounds. R^2: Substituting Group of **II** Series Compounds. R^3: Substituting Group of **III** Series Compounds. Reagents and conditions: (**a**) R^2OH, $SOCl_2$, 0 °C-reflux; (**b**) EDCI, HOBt, Et_3N, CH_2Cl_2, rt; (**c**) CH_3OH, NaOH, 65 °C, then HCl, H_2O. (**d**) R^2OH, DCC, DMAP, CH_2Cl_2, rt.

hydrolyzed to obtain hit compound **7**, which was then reacted with the above-mentioned alcohols in the presence of DCC as an ester-condensation agent to access the final products **II-4** and **II-5**. Subsequently, the classical amide condensation reaction was used to obtain compounds **III-1~III-22** because the initial substrate was **28**.

Vitro $P2Y_{14}R$ Inhibition and Structure–Activity Relationship

To evaluate the activity of the three series of compounds that we designed and synthesized, we conducted tests to determine the inhibitory effects of these compounds on cAMP production induced by the intracellular cAMP inducer forskolin (30 mM) in HEK293 cells stably expressing $P2Y_{14}R$. The inhibitory activities of these compounds were tested at a relatively high single inhibitor concentration (100 nM) to determine the most effective $P2Y_{14}R$ antagonist. The IC_{50} values of antagonists with more than 70% inhibition at 100 nM were further tested in the functional assay, and the results are presented in Tables 2–4, respectively. Structure–activity relationships (SAR) of these compounds were investigated.

In series **I**, the methyl group on the benzene ring of compound **7** was replaced with common electron-withdrawing and electron-donating substituents to obtain compound**s I-1~I-7**. As shown in Table 2, while compound **I-1** (inhibition = 82.67%, IC_{50} = 18.9 nM) with a hydrogen substitute had an inhibitory activity as hit compound **7**, the inhibitory activity of the other six compounds decreased to varying degrees (inhibition activity was between 34% and 64%), especially when an electron-withdrawing substituent was attached (inhibition of **I-2** with a methoxy group was 63.15% and **I-7** with a trifluoromethyl group was 34.81%). This could be due to changes in the electron density on the benzene ring, which prevented the new compounds from interacting with the surrounding residues through π–H and π–π interactions, as seen with compound **7** in Figure 6B. Subsequently, **I-8~I-15** were prepared by replacing the benzene ring with a heterocyclic ring. The introduction of heterocyclic or benzoheterocyclic rings did not significantly improve the antagonistic activities of the compounds. **I-8**, which has a furan ring (IC_{50} = 23.4 nM), showed slightly better activity than compound **7**.

https://doi.org/10.2147/DDDT.S497291

Table 2 In vitro $P2Y_{14}R$ Antagonistic Activity and cLogP Values of Compounds I-1~I-15

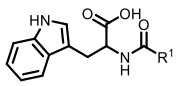

I-1~I-15

Compound	R^1	$P2Y_{14}R$ Antagonistic Activity		cLogP
		Inhibition at 100 nM (%)	IC_{50} (nM) [a]	
I-1	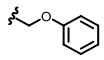	82.67	18.9±2.45	2.49
I-2	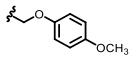	63.15	NT[c]	2.27
I-3	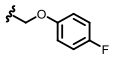	36.42	NT	2.88
I-4	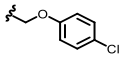	47.64	NT	3.39
I-5	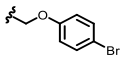	38.96	NT	3.19
I-6	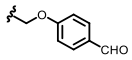	58.72	NT	2.15
I-7	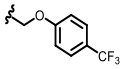	34.81	NT	3.23
I-8		73.61	23.4±0.78	2.23
I-9		68.02	NT	2.66

(*Continued*)

Table 2 (Continued).

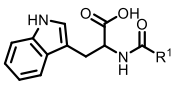

I-1~I-15

Compound	R^1	$P2Y_{14}R$ Antagonistic Activity		cLogP
		Inhibition at 100 nM (%)	IC_{50} (nM) [a]	
I-10		60.47	NT	1.98
I-11		10.73	NT	3.82
I-12	 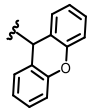 	40.62	NT	2.03
I-13		36.70	NT	2.80
I-14	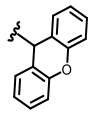	18.93	NT	4.15
I-15		23.65	NT	2.99
7 [b]		83.62	35.4±0.12	2.68
PPTN [b]		94.88	2.0±0.03	6.18

Notes: R^1: Substituting Group of **I** Series Compounds. [a] The results of three parallel tests are averaged, and the error is between 5% and 10%; [b] Positive control group; [c] NT is not tested.

https://doi.org/10.2147/DDDT.S497291

Table 3 In vitro $P2Y_{14}R$ Antagonistic Activity and cLogP Values of Compounds II-1~II-5

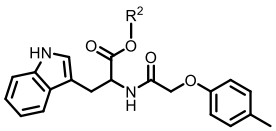

II-1~II-5

Compound	R^2	$P2Y_{14}R$ Antagonistic Activity		cLogP
		Inhibition at 100 nM (%)	IC_{50} (nM) [a]	
II-1		−20.03±1.25	NT[c]	3.12
II-2		−48.87±5.72	NT	3.61
II-3		109.94±3.17	1.2±0.11	3.77
II-4		57.55±2.78	NT	4.59
II-5		1.96±0.14	NT	4.67
7 [b]		83.62±1.97	35.4±1.12	2.68
PPTN [b]		94.88±5.68	2.0±0.03	6.18

Notes: R^2: Substituting Group of **II** Series Compounds. [a] The results of three parallel tests are averaged, and the error is between 5% and 10%; [b] Positive control group; [c] NT is not tested.

However, compared to **PPTN**, these compounds did not exhibit significantly higher antagonistic activity. To advance our research on $P2Y_{14}R$ antagonists, there is an urgent need to identify compounds that demonstrate antagonistic activity significantly superior to that of **PPTN**.

In series **II**, five diverse alcohols were used to cap the acid moiety of the hit compound **7** to access compounds **II-1~II-5**. As shown in Table 3, the inhibition activity almost completely disappeared when R^2 was methyl (**II-1**), ethyl (**II-2**), or cyclohexyl (**II-5**), and the inhibition activity decreased by half compared to that of hit compound **7** when R^2 was benzyl (**II-4**). However, compound **II-3** with R^2 as isopropyl, showed potent antagonistic activity, with an IC_{50} value of 1.2 nM. The results indicated that the size of the ester group had a significant effect on the antagonistic activity.

The mechanisms by which esterification and benzene ring substitution affect binding affinity and bioavailability at the molecular level are complex and multidimensional. Esterification modification may reduce hydrogen bonding or electrostatic interaction with the target protein by introducing ester groups to change the polarity and spatial configuration of the molecule, thereby affecting the binding affinity. At the same time, esterification modifications usually improve the lipid solubility of molecules, enhance their transmembrane ability and improve bioavailability. Benzene ring substitution

Table 4 In vitro $P2Y_{14}R$ Antagonistic Activity and cLogP Values of Compounds III-1~III-22

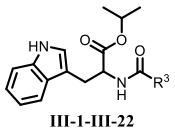

III-1-III-22

Compound	R^3	$P2Y_{14}R$ Antagonistic Activity		cLogP
		Inhibition at 100 nM (%)	IC_{50} (nM) [a]	
III-1	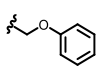	79.31±0.95	4.4±0.11	4.67
III-2	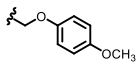	85.62±7.21	15.6±0.14	3.24
III-3	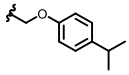	48.34±0.56	NT[c]	4.53
III-4	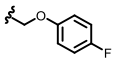	12.07±0.11	NT	3.34
III-5	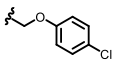	39.65±3.52	NT	4.17
III-6	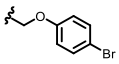	38.27±2.14	NT	4.45
III-7	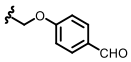	15.19±0.17	NT	3.39
III-8	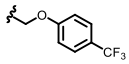	68.24±1.15	NT	4.17
III-9		77.34±0.74	21.61±0.21	3.26

(*Continued*)

https://doi.org/10.2147/DDDT.S497291

Table 4 (Continued).

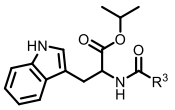

III-1-III-22

Compound	R^3	$P2Y_{14}R$ Antagonistic Activity		cLogP
		Inhibition at 100 nM (%)	IC_{50} (nM) [a]	
III-10		70.33±1.98	45.8±1.74	3.78
III-11		81.22±4.32	10.32±0.24	3.01
III-12		49.37±1.15	NT	3.02
III-13		11.28±0.36	NT	4.77
III-14		10.69±0.51	NT	2.92
III-15	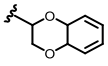	9.84±0.23	NT	2.93
III-16		67.57±1.94	NT	3.95
III-17		69.36±3.32	NT	3.67
III-18	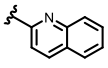	55.39±5.22	NT	4.07

(*Continued*)

Table 4 (Continued).

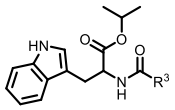

III-1-III-22

Compound	R^3	$P2Y_{14}R$ Antagonistic Activity		cLogP
		Inhibition at 100 nM (%)	IC_{50} (nM) [a]	
III-19	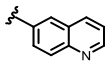	84.27±0.74	10.6	3.70
III-20	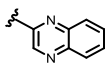	61.58±6.32	NT	3.28
III-21	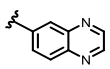	89.56±4.15	9.8	3.01
III-22	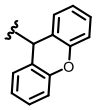	12.37±0.14	NT	4.88
II-3 [d]		109.94±3.17	1.2±0.11	3.77
7 [b]		83.62±2.21	35.4±1.12	2.68
PPTN [b]		94.88±4.56	2.02±0.01	6.18

Notes: R^3: Substituting Group of **III** Series Compounds. [a] The results of three parallel tests are averaged, and the error is between 5% and 10%; [b] Positive control group; [c] NT is not tested; [d] Structural information was found in Series **II.**

changes the electronic distribution and configuration of molecules through electronic and spatial effects, affecting the π-π accumulation or cation-π interaction with the target protein, thereby regulating the binding affinity. In addition, the nature of the substituents significantly affects the solubility and metabolic stability of the molecule, thus determining its bioavailability. Taken together, the synergistic effect of esterification modification and benzene ring substitution can play a key role in optimizing molecular efficacy and pharmacokinetic properties.

Since **II-3** exhibited potent inhibitory activity, it was selected as the lead compound to optimize series **III**. Thus, by maintaining the isopropyl group at R^2 and modifying R^3 substituents, compounds **III-1~III-22** were prepared. The methyl group on the benzene ring of compound **II-3** was replaced with common electron-withdrawing and electron-donating substituents to obtain compounds **III-1~III-8**. As shown in Table 4, no compounds in **III-1~III-8** showed better antagonistic activity than **II-3**. When the methyl group was replaced by hydrogen (**III-1**, IC_{50} = 4.4 nM) or methoxy (**III-2**, IC_{50} = 15.6 nM) groups, the compounds retained a certain degree of antagonistic activity. However, compared to **II-3**, the effect decreased several to dozens of times. When other electron-donating substituents, such as isopropyl (**III-3**), were introduced, the inhibitory activity obviously decreased (inhibition < 50%). In addition, when electron-withdrawing

https://doi.org/10.2147/DDDT.S497291

substituents, such as halogen (**III-4~III-6**) or formyl (**III-7**), were introduced, the inhibition activity also decreased significantly (inhibition < 40%), but the inhibition activity was retained when the methyl group was replaced by trifluoromethyl (**III-8**, inhibition = 68.24%). The above results confirmed that changing the electron cloud density on the benzene ring had no positive influence on antagonistic activity. This may be due to the electron-withdrawing substituents decreasing the electron density of the benzene ring through induction and conjugation effects, weakening its key interactions with the target protein (hydrogen bonding, π-π packing and cation-π interactions), thereby decreasing binding affinity. At the same time, electron-withdrawing substituents may introduce steric hindrance, which prevents the molecule from entering the target-binding pocket or interferes with its interaction with key residues. Subsequently, common heterocyclic and benzoheterocyclic rings with various biological activities were introduced into the system to replace the benzene ring. As expected, when R^3 was furan (**III-9**, IC_{50} = 21.6 nM), thiophene (**III-10**, IC_{50} = 45.8 nM), pyridine (**III-11**, IC_{50} = 10.3 nM), or indole (**III-16**, inhibition = 67.57%), the antagonistic activity still remained though declined to some extent compared to **II-3**. However, when thiazole (**III-12**), benzo[*b*]thiophene (**III-13**), benzo[*d*][1,3] dioxole (**III-14**), or 2,3-dihydrobenzo[*b*][1,4]dioxine (**III-15**) were introduced, the antagonistic activity was significantly reduced, which may have been influenced by the conjugated π-electron systems. Interestingly, when quinoline was introduced at different positions in the system, the change in the antagonistic activity of **III-17~III-19** was significant. The main performance was 2-position < 3-position < 6-position, indicating that the system connected directly to benzene was favorable for improving the antagonistic activity. The antagonistic activity of compound **III-21** with a 6-substituted quinoxaline structure was better than that of compound **III-20** with 2-substituted quinoxaline, and **III-22** with 9-substituted-9*H*-xanthene lost its inhibitory activity, which further confirmed the importance of the benzene ring. However, we found that after the structural optimization of the **III** series, the antagonistic activity of the compounds obtained in **III** series was not as good as that of the lead compound **II-3**.

After the optimization and structure–activity relationship discussion of three series of novel $P2Y_{14}R$ antagonists, we found that compound **II-3** had the strongest antagonistic activity against $P2Y_{14}R$, which was better than **PPTN** and lead compound **7**. In some cases, the introduction of an ester group may optimize the spatial configuration of the molecule or enhance the hydrophobic interaction, which in turn improves the binding capacity to the target. In terms of druggability, esterification modification usually significantly improves the lipid solubility of molecules, enhances their transmembrane ability and oral absorption, thereby improving bioavailability. In addition, esterification may also reduce the toxicity and irritation of the molecule, and improve its formulation stability. Therefore, compound **II-3** was selected for further study.

Molecular Docking

During the optimization process, compound **II-3** was identified as a $P2Y_{14}R$ antagonist with high antagonistic activity and as a new scaffold. Molecular docking was employed to illuminate the prominent antagonistic activity of compound **7** with the novel scaffold; compound **II-3** was used as an example, and **PPTN** was used as a control. The protein structure used for molecular docking was the $hP2Y_{14}R$ structure reported by Jacobson et al.

The binding mode and interactions between compound **II-3** and $hP2Y_{14}R$ through molecular docking are shown in Figure 8A. It can be clearly seen that compound **II-3** can be well fixed in the hydrophobic pocket of $hP2Y_{14}R$. The indole moiety of **II-3** was directed to the extracellular solvent area and formed H-bonds with Thr157 at a distance of 3.02 Å. The 4-methylbenzene moiety entered the hydrophobic pocket and interacted with Ile162 via π–H interactions at a distance of 4.28 Å. It can also be seen that the amide bond of compound **II-3** formed H-bonds with Cys161 in $P2Y_{14}R$ at a distance of 3.19 Å, which indicates that the amide bond will remain in novel antagonists not only as a tool to connect different pharmacophores but also play a key role in improving the antagonistic activity of new compounds. As a linker, the amide bond maintains the spatial arrangement of the pharmacophore through its rigidity and planarity, ensuring that it is precisely matched to the active site of the target protein, thereby enhancing the binding affinity. Secondly, the amide bond itself is polar, and its carbonyl oxygen and amino hydrogen can act as hydrogen bond acceptors and donors, respectively, to form stable hydrogen bond interactions with residues in the target protein, further consolidating the binding of the molecule to the target. In addition, the resonance effect of amide bonds gives it partial double bond properties, which enhances the conformational stability of the molecule and reduces the distribution of inactive conformations. In addition, the carboxyl group of compound **II-3** formed H-bonds with Arg263 at a distance of 2.89

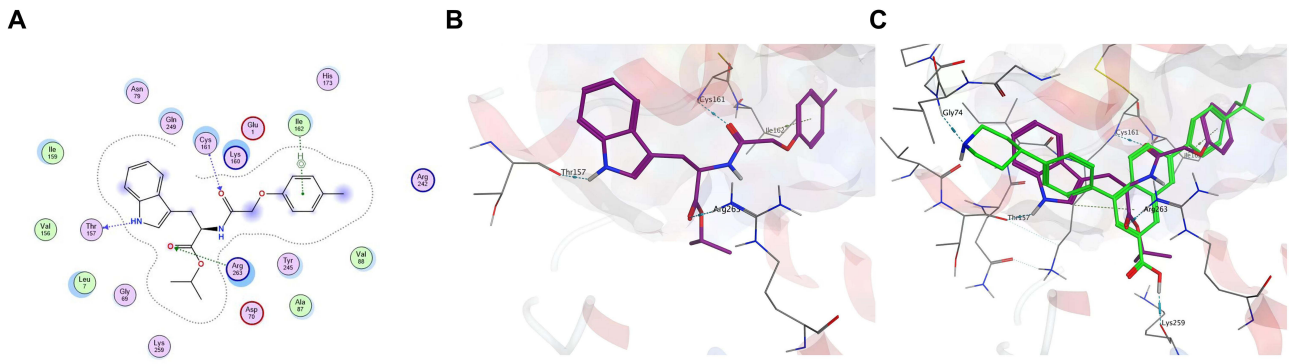

Figure 8 Binding modes of $hP2Y_{14}R$ antagonists and their interactions. (**A**) 2D binding model and the interactions between compound **II-3** and $hP2Y_{14}R$. (**B**) 3D binding model and the interactions between compound **II-3** (purple-colored moiety) and $hP2Y_{14}R$. (**C**) Docking pose overlay of **PPTN** (green-colored moiety) and **II-3** (purple-colored moiety) in $hP2Y_{14}R$.

Å, whereas compound **7** did not form any interactions with the residues surrounding $P2Y_{14}R$, indicating that the carboxyl group is essential for binding, which is consistent with the results of the SAR studies. This further confirmed that the introduction of ester groups can optimize the spatial configuration and electron distribution of the molecule, so that it can better bind to the binding pocket of the target protein, and ester group modifications may also play a role through the prodrug strategy, and be metabolized into a more active carboxylic acid form in vivo, thereby enhancing antagonistic activity.

A 3D docking model of compounds **II-3** and $hP2Y_{14}R$, as well as the crystallographic overlap between **II-3** and **PPTN**, is displayed in Figure 8B and C. Compounds **II-3** (purple carbons) and **PPTN** (green carbons) were docked on the same active site through an analogous binding pattern, and the degree of crystallographic overlap between the two compounds was considerable.

Binding Mode Analysis

We conducted molecular dynamics simulations of the complex, as shown in Figure 9A–E. In the 100 ns simulation, the Rg fluctuation of the complex fluctuated slightly due to the system equilibrium in the early stage of the simulation, and then the amplitude gradually decreased. At 100 ns, the Rg value of the complex was 1.855 nm. Similarly, the RMSD value of the complex fluctuated in the early stage of the simulation. With the extension of the simulation time, the fluctuation amplitude of the RMSD value decreased, and finally the RMSD value was 0.824 nm. RMSF reflects the flexibility of amino acid sites. As shown in Figure 9C, except for the fluctuations of the residues at the N-terminal and C-terminal, the RMSF of most residues is less than 0.4 nm. The residues show overall stability, with only a few residues showing fluctuations.

In addition, we analyzed and obtained the hydrogen bond information formed between the protein and the ligand. As shown in Figure 9D, in the 100 ns molecular dynamics simulation, the ligand and the protein can form hydrogen bond interactions, and the number of hydrogen bonds formed between the protein and the ligand ranges from 0 to 5. In 100 ns, the average number of hydrogen bonds is 0.69, indicating a relatively limited number of hydrogen bonds. SASA can reflect the surface area of the protein exposed to the solvent and also the stability of the protein structure. As shown in Figure 9E, combined with the SASA graph, in the middle and later stages of the simulation, the SASA value was maintained at around 115 nm2, and the protein structure was basically stable.

Selectivity versus Other P2Y Receptor Subtypes

To gain insight into the selectivity of **II-3**, we assessed **II-3** for receptor subtypes that share the greatest sequence homology with $P2Y_{14}R$, including $P2Y_1R$, $P2Y_2R$, $P2Y_4R$, $P2Y_6R$, and $P2Y_{12}R$.[29,30,35] The receptors exhibit a certain degree of structural similarity at the molecular level, primarily characterized by the presence of seven transmembrane α-helical regions (TM1–TM7), which together form a binding pocket for the ligands. Moreover, there is a high degree of sequence conservation in key transmembrane segments such as TM3, TM6, and TM7.[36] As shown in Table 5, **II-3**

https://doi.org/10.2147/DDDT.S497291

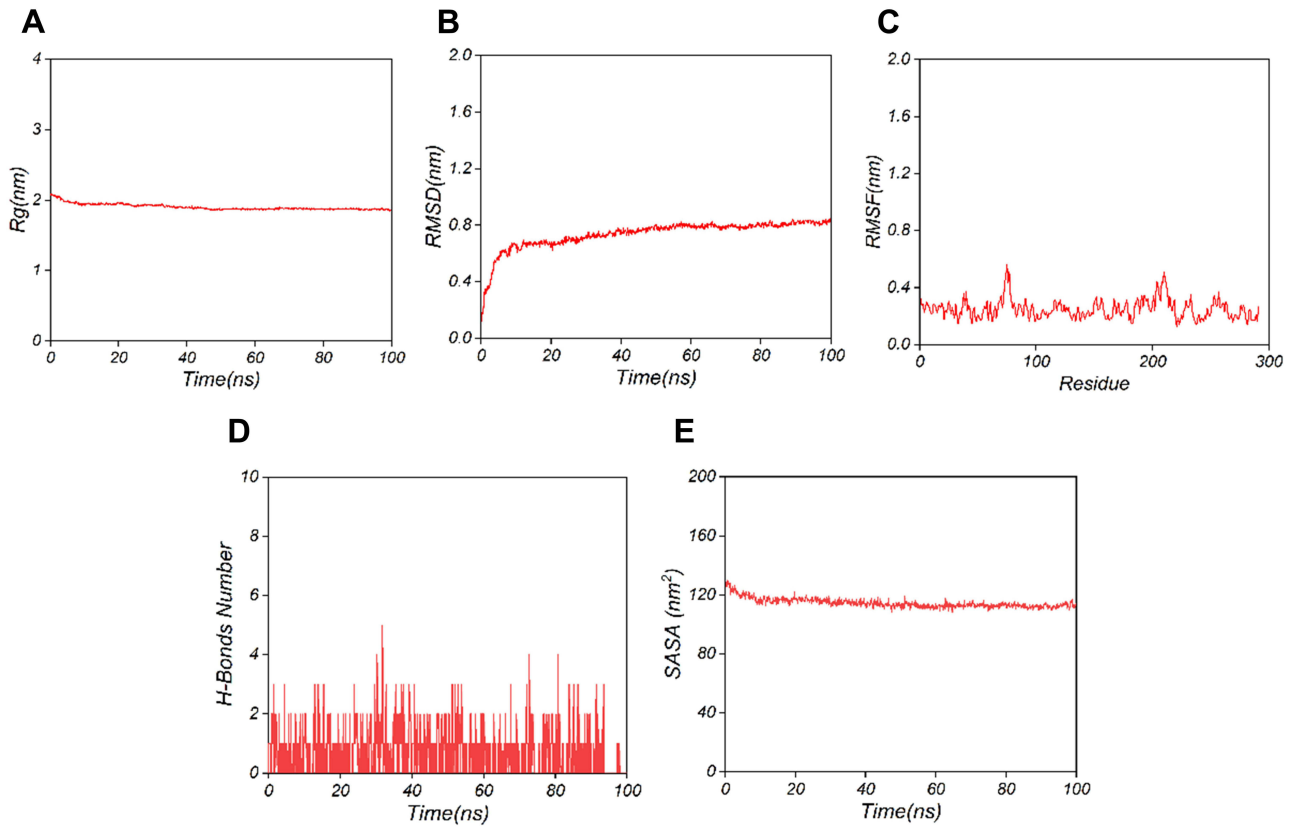

Figure 9 Binding modes of hP2Y$_{14}$R antagonists and their interactions. (**A**) The Rg results of complex; (**B**) The RMSD results of complex; (**C**) The RMSF results of complex; (**D**) The H-Bonds Number results of complex; (**E**) The SASA results of complex.

showed a particularly high selectivity compared to P2Y$_1$R, P2Y$_2$R, P2Y$_4$R, P2Y$_6$R, and P2Y$_{12}$R, suggesting that **II-3** displays P2Y$_{14}$R selectivity. The high selectivity of **II-3** makes it a promising anti-inflammatory agent that can modulate the immune system more accurately and with a lower risk of side effects.

In vitro ADMET Study of II-3

Experimental studies on the absorption, distribution, metabolism, excretion, and toxicity (ADMET) properties of **II-3** were conducted and are summarized in Table 6. **II-3** showed IC$_{50}$ values of >25 μM for all five CYPs tested. It was stable in simulated intestinal and gastric fluids and demonstrated excellent stability in human liver microsomes with a half-life of 352 min. The stability of the compound across various simulated environments and its low potential for CYP-mediated drug interactions suggest good metabolic stability and reduced risk of adverse effects. Assays for the inhibition of hERG channels indicated that **II-3** had a few cardiotoxic side effects (IC$_{50}$ > 50 μM). Thus, these attributes position **II-3** as are promising candidates for further development.

PK/PD Evaluation of II-3

The pharmacokinetic profiles of **II-3** in mice were comprehensively evaluated and are summarized in Table 7. Pharmacokinetic evaluation of **II-3** in Sprague-Dawley (SD) mice revealed robust absorption and distribution

Table 5 The Selectivity of II-3 to Different P2Y Receptors

P2YR	P2Y$_{14}$R	P2Y$_1$R	P2Y$_2$R	P2Y$_4$R	P2Y$_6$R	P2Y$_{12}$R
Activity	1.20±0.11	>10 uM	4.2 uM	>10 uM	>10 uM	>10 uM

Notes: Data are expressed as mean ± SEM (n ≥ 3).

Table 6 In vitro ADMET Profile of II-3

Parameters		Parameters	
CYP1A2 (IC_{50}, μM)	> 50	Simulated intestinal fluid ($t_{1/2}$, min)	> 300
CYP2C9 (IC_{50}, μM)	> 50	Simulated gastric fluid ($t_{1/2}$, min)	> 3000
CYP2C19 (IC_{50}, μM)	31.5	Human liver microsomal stability (Cl_{int}(μL/(mg•min))	14.6
CYP2D6 (IC_{50}, μM)	27.4		
CYP3A4 (IC_{50}, μM)	> 50	Human liver microsomal stability ($t_{1/2}$, min)	352
hERG (IC_{50}, μM)	> 50		

Notes: Data are expressed as mean ± SEM (n ≥ 6).

Table 7 Pharmacokinetic Profiles of II-3

Dose (mg/kg)	C_{max}(ng/mL)	$T_{1/2}$ (h)	T_{max}(min)	$AUC_{0\text{-}24h}$(μg/(L•h))	CL (mL/min/kg)	F (%)
iv (10 mg/kg)	1845 ± 12	2.2 ± 0.7	48 ±12	2456 ± 31	5.5 ± 0.3	–
po (20 mg/kg)	2561 ± 33	6.1 ± 1.0	72 ± 8	3258 ± 74	32.3 ± 2.0	39

Notes: Data are expressed as mean ± SEM (n ≥ 6). Abbreviations: C_{max}, maximum blood drug concentration; $T_{1/2}$, terminal half-life; T_{max}, peak time of blood drug concentration after administration; AUC, area under the plasma drug concentration–time curve; CL, plasma clearance level; iv, intravenous injection; po, oral administration.

characteristics. Oral dosing at 20 mg/kg yielded a peak concentration (C_{max}) of 2561 ng/mL, indicative of efficient absorption. The time to reach C_{max} (T_{max}) was 72 min, and the area under the curve from 0 to 24 hours ($AUC_{0\text{-}24h}$) was 3258 μg/(L·h), reflecting the exposure of the compound over the initial dosing interval. The half-life ($T_{1/2}$) of 6.1 hours suggests that **II-3** was cleared at a moderate rate. A moderate bioavailability (F) of 39% implies that a significant portion of the oral dose is available in systemic circulation, which is beneficial for ensuring therapeutic plasma levels. Upon intravenous administration at 10 mg/kg, **II-3** demonstrated a slightly lower C_{max} (1845 ng/mL), T_{max} (48 min), and $AUC_{0\text{-}24h}$ (2456 μg/(L·h)), suggesting rapid distribution and elimination. The shorter half-life (2.2 hours via the intravenous route underscores the rapid clearance of the compound from the systemic circulation.

In vivo Efficacy of II-3 in the LPS-Induced Mouse ALI Model

Based on in vitro results, an LPS-induced ALI mouse model was used to investigate the therapeutic potential of **II-3** in vivo. At present, the treatment of ALI mainly involves supportive therapies (respiratory and hemodynamic support) and drug treatments (anti-inflammatory drugs, antioxidants, and cytoprotective agents), but there are no approved drugs specifically for ALI.[37] Dexamethasone (DXMS), a clinical glucocorticoid, was used as an anti-inflammatory agent for positive comparison. The anti-inflammatory effects of $P2Y_{14}R$ have been demonstrated in a range of inflammatory diseases (such as AGA and IBD) highlighting its potential for the treatment of ALI.[15,34] However, the pro-inflammatory mechanisms of $P2Y_{14}R$ in ALI have not been fully elucidated. In this study, we utilized single-cell sequencing technology to obtain a single-cell atlas of lung tissue from both normal mice and LPS-induced ALI mice. Our observations revealed an increase in immune cells within the lung tissue of mice under disease conditions, along with an increased co-localization of $P2Y_{14}R$ and immune cells, with macrophages showing a particularly noticeable co-localization with $P2Y_{14}R$ (Figure 10A). This suggests that $P2Y_{14}R$ may play a crucial role in the inflammatory response during ALI. Consequently, we employed immunofluorescence technology to co-localize macrophages and $P2Y_{14}R$ in lung tissue (Figure 10B), and our findings were consistent with those obtained from single-cell sequencing. This provides a visual and direct evidence supporting the role of $P2Y_{14}R$ in mediating inflammation. In summary, our research has provided critical insights into the pathophysiology of ALI and has suggested that targeting $P2Y_{14}R$ could represent a

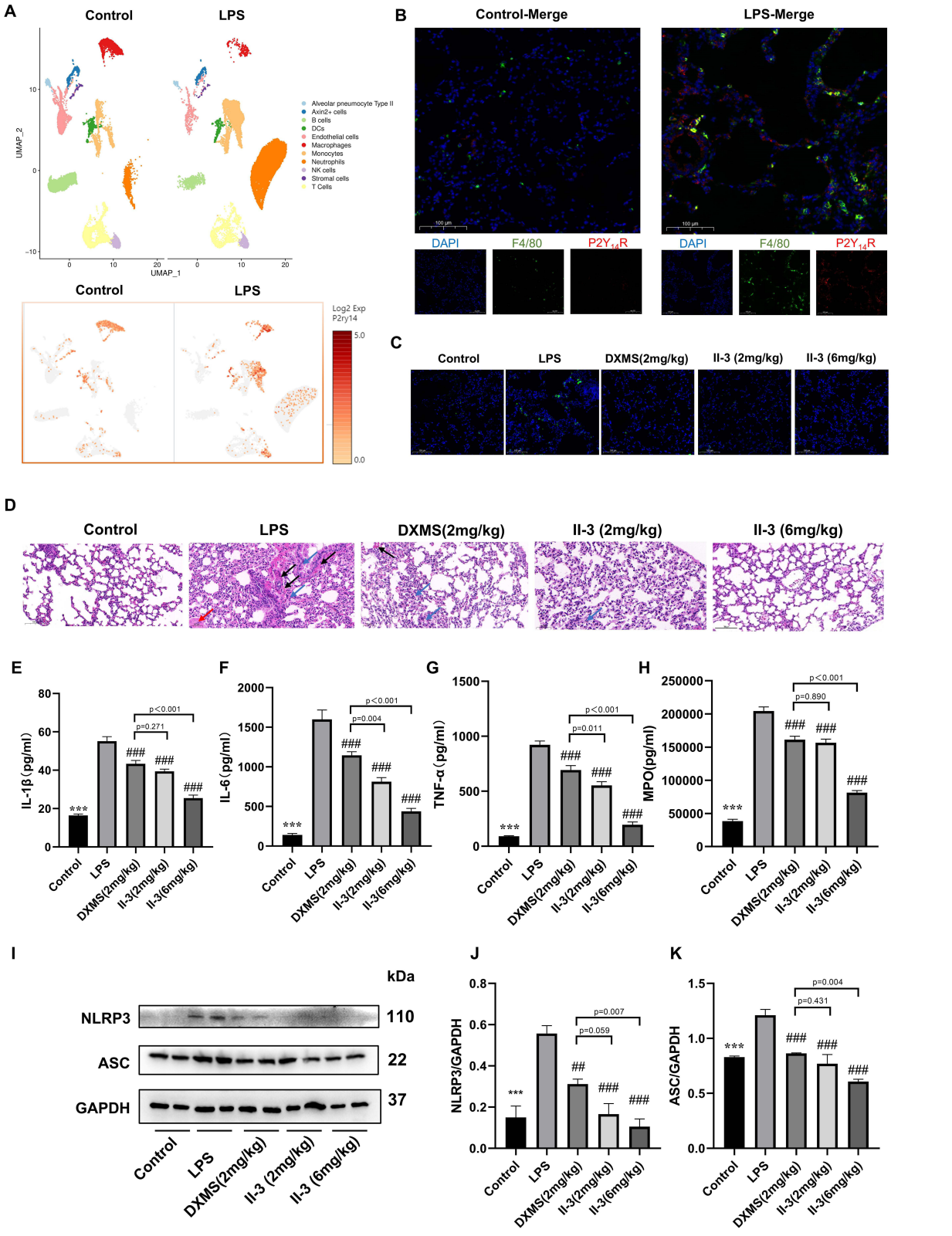

Figure 10 II-3 attenuated LPS-induced lung inflammation in mice. (**A**) Comparison of the differential expression of $P2Y_{14}R$ in monocytes/macrophages between normal mouse (Control) and LPS-induced ALI mouse (LPS) in lung tissue, with data derived from our self-built single-cell database. (**B**) Co-localization of $P2Y_{14}R$ and macrophages under different disease conditions (scale bar = 100 μm). (**C**) Immunofluorescence analysis of F4/80 in lung tissue sections (scale bar = 100 μm). (**D**) H&E staining of lung sections. Red arrows: intravascular congestion; black arrows: pulmonary interstitial hemorrhage; blue arrows:neutrophilic infiltration. (**E**–**H**) Protein levels of (**E**) IL-1β, (**F**) IL-6, and (**G**) TNF-α in the BALF and (**H**) MPO in lung tissue after various treatments (n = 6). (**I**–**K**) Western blotting analysis of NLRP3 inflammasome pathway proteins. Each bar represents the mean ± SEM of three independent experiments. One-way analysis of variance (ANOVA) was performed after the assessment of normal distribution and homogeneity of variance test. ***$p < 0.001$ compared with the control group. $^{\#\#}p < 0.01$ and $^{\#\#\#}p < 0.001$ compared with the LPS only group.

https://doi.org/10.2147/DDDT.S497291

promising strategy for the development of novel therapeutic interventions. Our findings underscore the potential of modulating $P2Y_{14}R$ signaling as a means to mitigate the inflammatory cascade in ALI, paving the way for future studies aimed at exploring this pathway's role and the efficacy of related treatments.

Next, we evaluated the efficacy of the selected $P2Y_{14}R$ antagonists, By immunofluorescence, we observed an improvement in pulmonary macrophage infiltration following drug administration (Figure 10C). Additionally, H&E staining revealed pronounced pathological changes in the LPS-induced group, including intravascular congestion (red arrows), pulmonary interstitial hemorrhage (black arrows), and neutrophilic infiltration (blue arrows). DXMS treatment (2 mg/kg) mitigated these effects, resulting in a reduction in inflammatory cell infiltration and less severe hemorrhage and congestion. Remarkably, **II-3** demonstrated a superior efficacy against DXMS. At a low dose of 2 mg/kg, **II-3** significantly reduced immune cell infiltration with minimal parenchymal lesions. A high dose of 6 mg/kg further decreased inflammatory cell infiltration and preserved the alveolar structure more effectively than did DXMS (Figure 10D).

Macrophages and neutrophils participate in the development of ALI, and activated macrophages can release inflammatory mediators and recruit neutrophils to amplify the inflammatory response.[19,20] To evaluate the anti-inflammatory effects of **II-3**, we measured the BALF levels of the pro-inflammatory cytokines IL-1β, IL-6, and TNF-α, which were significantly upregulated in the ALI model (Figure 10E–G). Pretreatment with II-3 notably reversed the LPS-induced increase in cytokine levels, with outcomes surpassing those of the DXMS group. Additionally, MPO is a key neutrophil enzyme that induces inflammation and is released by neutrophils.[38] We measured MPO levels in the lung tissue to assess **II-3**'s impact on neutrophil activity. The results showed that II-3 significantly lowered MPO levels triggered by LPS (Figure 10H). Collectively, these results indicate that **II-3** plays a protective role in lung inflammation by reducing immune cell infiltration, inflammatory cytokine levels, and pulmonary pathological changes in the LPS-induced ALI model.

It is noteworthy that recent studies have reported that $P2Y_{14}R$ antagonists significantly reduce pulmonary inflammation and tissue damage in ALI by inhibiting the activation of the NLRP3 inflammasome signaling pathway, decreasing the release of inflammatory factors, and reducing immune cell infiltration. The NLRP3 inflammasome, a multiprotein complex, plays a crucial role in cellular inflammatory responses and cell death. $P2Y_{14}R$ antagonists may offer protective effects against ALI by influencing this signaling pathway. Additionally, the activation of $P2Y_{14}R$ may be involved in modulating immune-inflammatory stress responses. In this study, we further investigated the inhibitory effect of $P2Y_{14}R$ antagonists on the NLRP3 inflammasome pathway. Our observations revealed that $P2Y_{14}R$ antagonists significantly reduced the activation of the NLRP3 inflammasome and the release of related inflammatory factors, thereby alleviating the inflammatory response (Figure 10I–K). These results are consistent with previous studies, indicating that $P2Y_{14}R$ plays a significant role in regulating inflammatory responses, and its antagonists may exert anti-inflammatory effects by inhibiting the activation of the NLRP3 inflammasome signaling pathway. Moreover, our findings further support the potential of $P2Y_{14}R$ as a therapeutic target for ALI.

Conclusion

In conclusion, we have designed a series of *N*-acyl tryptophan derivatives that have been identified as novel and potent $P2Y_{14}R$ antagonists based on compound **7**. Compound **II-3** showed the most promising antagonistic activity. The solubility and bioavailability of compound **II-3** were better than **PPTN** owing to the elimination of zwitterionic characteristics, and its druggability was significantly improved. Optimized compound **II-3** (IC_{50} = 1.2 nM) also displayed a more potent $P2Y_{14}R$ antagonistic activity than **PPTN** (IC_{50} = 2.0 nM). The high selectivity of compound **II-3** against P2Y-type receptors homologous to $P2Y_{14}R$, the high selectivity of II-3 for $P2Y_{14}R$ was further confirmed. In the pharmacokinetic experiments, compound **II-3** showed excellent bioavailability (F = 39%). Good plasma clearance and half-life indicated that compound **II-3** was remarkably stable in vitro and *vivo*. Assays for the inhibition of the cytochrome P450 and hERG channels indicated that compound **II-3** had few cardiotoxic side effects in vivo. Using single-cell sequencing and immunofluorescence techniques, this study for the first time reveals the specific high expression of $P2Y_{14}R$ in macrophages of ALI lung tissue, and confirms that II-3 effectively targets $P2Y_{14}R$, inhibiting NLRP3 inflammasome activation and curbing the release of key inflammatory cytokines like IL-1β, IL-6, and TNF-α.

This action results in a dual anti-inflammatory effect, both reducing immune cell infiltration and inflammatory signaling. Importantly, II-3 was found to notably ameliorate lung pathology and lower pro-inflammatory cytokine levels in an ALI model, outperforming dexamethasone (DXMS). Overall, this study innovatively combines single-cell spatial profiling to analyze target distribution, providing a new direction for the development of specific anti-ALI drugs, compound **II-3** has clear targets, excellent anti-inflammatory activity in vivo, druggability, and low liver toxicity. In addition, the synthesis route and post-treatment of compound **II-3** were relatively simple and convenient for mass production. Compound **II-3** with potent $P2Y_{14}R$ antagonistic activity, provides a reliable therapeutic strategy for efficient treatment of inflammatory diseases and is a promising candidate for further research.

Ethical Approval Statement

All animal experiments were performed following the Zhengzhou University and national guidelines and regulations. The full procedures were approved by the Institutional Animal Care and Use Committee of Zhengzhou University, with the ethical approval code being 23-IACUC-Y008.

Acknowledgments

This work was supported by Key Research and Development Project of Henan (No.241111313600), Natural Science Foundation of Henan (No.232300421086), Henan Medical Science and Technology Program (No. SBGJ202302102), Zhongyuan Science and Technology Innovation Young Top Talents Program and Joint Fund of Henan Provincial Science and Technology Research (No.225200810114, 232301420055, 242301420074).

Author Contributions

All authors contributed to the study design, execution, acquisition of data, data analysis, drafting or revision of the article, agreed on the journal to which the article will be submitted, gave final approval of the version to be published, and agreed to be accountable for all aspects of the work.

Disclosure

The authors declare that they have no known competing financial interests or personal relationships that could influence the work reported in this study.

References

1. Conroy S, Kindon N, Kellam B, Stocks MJ. Drug-like antagonists of P2Y receptors-from lead identification to drug development. *J Med Chem*. 2016;59(22):9981–10005. doi:10.1021/acs.jmedchem.5b01972
2. Abbracchio MP, Burnstock G, Boeynaems JM, et al. International Union of Pharmacology LVIII: update on the P2Y G protein-coupled nucleotide receptors: from molecular mechanisms and pathophysiology to therapy. *Pharmacol Rev*. 2006;58(3):281–341. doi:10.1124/pr.58.3.3
3. Burnstock G. Physiology and pathophysiology of purinergic neurotransmission. *Physiol Rev*. 2007;87(2):659–797. doi:10.1152/physrev.00043.2006
4. Burnstock G. Purinergic nerves. *Pharmacol Rev*. 1972;24(3):509–581. doi:10.1016/S0031-6997(25)06930-3
5. Burnstock G. Introduction: P2 receptors. *Curr Top Med Chem*. 2004;4(8):793–803. doi:10.2174/1568026043451014
6. Burnstock G. Purine and pyrimidine receptors. *Cell Mol Life Sci*. 2007;64(12):1471–1483. doi:10.1007/s00018-007-6497-0
7. Ko H, Fricks I, Ivanov AA, Harden TK, Jacobson KA. Structure-activity relationship of uridine 5'-diphosphoglucose analogues as agonists of the human P2Y14 receptor. *J Med Chem*. 2007;50(9):2030–2039. doi:10.1021/jm061222w
8. Das A, Ko H, Burianek LE, Barrett MO, Harden TK, Jacobson KA. Human P2Y(14) receptor agonists: truncation of the hexose moiety of uridine-5'-diphosphoglucose and its replacement with alkyl and aryl groups. *J Med Chem*. 2010;53(1):471–480. doi:10.1021/jm901432g
9. Gauthier JY, Belley M, Deschênes D, et al. The identification of 4,7-disubstituted naphthoic acid derivatives as UDP-competitive antagonists of P2Y14. *Bioorg Med Chem Lett*. 2011;21(10):2836–2839. doi:10.1016/j.bmcl.2011.03.081
10. Chambers JK, Macdonald LE, Sarau HM, et al. A G protein-coupled receptor for UDP-glucose. *J Biol Chem*. 2000;275(15):10767–10771. doi:10.1074/jbc.275.15.10767
11. Carter RL, Fricks IP, Barrett MO, et al. Quantification of Gi-mediated inhibition of adenylyl cyclase activity reveals that UDP is a potent agonist of the human P2Y14 receptor. *Mol Pharmacol*. 2009;76(6):1341–1348. doi:10.1124/mol.109.058578
12. Fricks IP, Carter RL, Lazarowski ER, Harden TK. Gi-dependent cell signaling responses of the human P2Y14 receptor in model cell systems. *J Pharmacol Exp Ther*. 2009;330(1):162–168. doi:10.1124/jpet.109.150730
13. Li H, Jiang W, Ye S, et al. P2Y(14) receptor has a critical role in acute gouty arthritis by regulating pyroptosis of macrophages. *Cell Death Dis*. 2020;11(5):394. doi:10.1038/s41419-020-2609-7
14. Lu R, Wang Y, Liu C, et al. Design, synthesis and evaluation of 3-amide-5-aryl benzoic acid derivatives as novel P2Y(14)R antagonists with potential high efficiency against acute gouty arthritis. *Eur J Med Chem*. 2021;216:113313. doi:10.1016/j.ejmech.2021.113313

15. Liu C, Wang H, Han L, et al. Targeting P2Y(14)R protects against necroptosis of intestinal epithelial cells through PKA/CREB/RIPK1 axis in ulcerative colitis. *Nat Commun*. 2024;15(1):2083. doi:10.1038/s41467-024-46365-x
16. Xu J, Morinaga H, Oh D, et al. GPR105 ablation prevents inflammation and improves insulin sensitivity in mice with diet-induced obesity. *J Immunol*. 2012;189(4):1992–1999. doi:10.4049/jimmunol.1103207
17. Sesma JI, Weitzer CD, Livraghi-Butrico A. et al. UDP-glucose promotes neutrophil recruitment in the lung. *Purinergic Sig*. 2016;12(4):627–635. doi:10.1007/s11302-016-9524-5
18. Gao ZG, Ding Y, Jacobson KA. UDP-glucose acting at P2Y14 receptors is a mediator of mast cell degranulation. *Biochem Pharmacol*. 2010;79 (6):873–879. doi:10.1016/j.bcp.2009.10.024
19. Azroyan A, Cortez-Retamozo V, Bouley R, et al. Renal intercalated cells sense and mediate inflammation via the P2Y14 receptor. *PLoS One*. 2015;10(3):e0121419. doi:10.1371/journal.pone.0121419
20. Battistone MA, Mendelsohn AC, Spallanzani RG, et al. Proinflammatory P2Y14 receptor inhibition protects against ischemic acute kidney injury in mice. *J Clin Invest*. 2020;130(7):3734–3749. doi:10.1172/jci134791
21. Kinoshita M, Nasu-Tada K, Fujishita K, Sato K, Koizumi S. Secretion of matrix metalloproteinase-9 from astrocytes by inhibition of tonic P2Y14-receptor-mediated signal(s). *Cell Mol Neurobiol*. 2013;33(1):47–58. doi:10.1007/s10571-012-9869-4
22. Mao S, Liu W, Wang X, et al. Design, synthesis and anti-inflammatory evaluation of 3-substituted 5-amidobenzoate derivatives as novel P2Y(14) receptor antagonists via structure-guided molecular hybridization. *J Med Chem*. 2025;68(3):2483–2503. doi:10.1021/acs.jmedchem.4c01539
23. Guay D, Beaulieu C, Belley M, et al. Synthesis and SAR of pyrimidine-based, non-nucleotide P2Y14 receptor antagonists. *Bioorg Med Chem Lett*. 2011;21(10):2832–2835. doi:10.1016/j.bmcl.2011.03.084
24. Robichaud J, Fournier JF, Gagné S, et al. Applying the pro-drug approach to afford highly bioavailable antagonists of P2Y(14). *Bioorg Med Chem Lett*. 2011;21(14):4366–4368. doi:10.1016/j.bmcl.2010.12.113
25. Barrett MO, Sesma JI, Ball CB, et al. A selective high-affinity antagonist of the P2Y14 receptor inhibits UDP-glucose-stimulated chemotaxis of human neutrophils. *Mol Pharmacol*. 2013;84(1):41–49. doi:10.1124/mol.113.085654
26. Junker A, Balasubramanian R, Ciancetta A, et al. Structure-based design of 3-(4-Aryl-1H-1,2,3-triazol-1-yl)-biphenyl derivatives as P2Y14 receptor antagonists. *J Med Chem*. 2016;59(13):6149–6168. doi:10.1021/acs.jmedchem.6b00044
27. Zhang Z, Hao K, Li H, et al. Design, synthesis and anti-inflammatory evaluation of 3-amide benzoic acid derivatives as novel P2Y(14) receptor antagonists. *Eur J Med Chem*. 2019;181:111564. doi:10.1016/j.ejmech.2019.111564
28. Jung YH, Yu J, Wen Z, et al. Exploration of alternative Scaffolds for P2Y(14) receptor antagonists containing a biaryl core. *J Med Chem*. 2020;63 (17):9563–9589. doi:10.1021/acs.jmedchem.0c00745
29. Wang W, Liu C, Li H, et al. Discovery of novel and potent P2Y(14)R antagonists via structure-based virtual screening for the treatment of acute gouty arthritis. *J Adv Res*. 2020;23:133–142. doi:10.1016/j.jare.2020.02.007
30. Wang YH, Zhou MZ, Ye T, et al. Discovery of a series of 5-amide-1H-pyrazole-3-carboxyl derivatives as potent P2Y(14)R antagonists with anti-inflammatory characters. *J Med Chem*. 2022;65(23):15967–15990. doi:10.1021/acs.jmedchem.2c01632
31. Kalsi N, Gopalakrishnan C, Rajendran V, Purohit R. Biophysical aspect of phosphatidylinositol 3-kinase and role of oncogenic mutants (E542K & E545K). *J Biomol Struct Dyn*. 2016;34(12):2711–2721. doi:10.1080/07391102.2015.1127774
32. Singh R, Purohit R. Computational analysis of protein-ligand interaction by targeting a cell cycle restrainer. *Comput Methods Programs Biomed*. 2023;231:107367. doi:10.1016/j.cmpb.2023.107367
33. Bhardwaj VK, Purohit R. A comparative study on inclusion complex formation between formononetin and β-cyclodextrin derivatives through multiscale classical and umbrella sampling simulations. *Carbohydr Polym*. 2023;310:120729. doi:10.1016/j.carbpol.2023.120729
34. Liu W, Mao S, Wang Y, et al. Discovery of N-substituted acetamide derivatives as promising P2Y(14)R antagonists using molecular hybridization based on crystallographic overlay. *J Med Chem*. 2024;67(12):10233–10247. doi:10.1021/acs.jmedchem.4c00555
35. Zhao Y, Han B, Wei Z, et al. Discovery of a potent, highly selective, and in vivo anti-inflammatory efficacious, P2Y(6)R antagonist with a novel quinoline-pyrazole scaffold. *Eur J Med Chem*. 2024;279:116890. doi:10.1016/j.ejmech.2024.116890
36. Burnstock G, Knight GE. Cellular distribution and functions of P2 receptor subtypes in different systems. *Int Rev Cytol*. 2004;240:31–304. doi:10.1016/s0074-7696(04)40002-3
37. Zhang J, Guo Y, Mak M, Tao Z. Translational medicine for acute lung injury. *J Transl Med*. 2024;22(1):25. doi:10.1186/s12967-023-04828-7
38. Siraki AG. The many roles of myeloperoxidase: from inflammation and immunity to biomarkers, drug metabolism and drug discovery. *Redox Biol*. 2021;46:102109. doi:10.1016/j.redox.2021.102109